

Elemental analysis and mapping of Chandrayaan-2 Large Area Soft X-ray Spectrometer Data

Abstract—The Chandrayaan-2 mission’s CLASS (Chandrayaan-2 Large Area Soft X-ray Spectrometer) instrument has provided a wealth of data for understanding the elemental composition of the lunar surface. In this study, we analyzed extensive CLASS instrument datasets to determine elemental abundances across various lunar regions using the XSPEC software. These abundances were mapped onto a lunar albedo map to correlate elemental distribution with surface reflectance properties. Additionally, we explored sub-pixel resolution enhancement techniques for these elemental abundance maps, leveraging machine learning methodologies to improve spatial resolution from 12.5 km to 2 km. Our approach highlights the potential of integrating traditional spectrometry analysis with modern machine learning techniques to derive finer spatial details, advancing our understanding of the Moon’s compositional heterogeneity and geological evolution.

I. INTRODUCTION

The Chandrayaan-2 mission, launched by the Indian Space Research Organisation (ISRO), represents a significant milestone in lunar exploration. Equipped with state-of-the-art instruments, the mission aims to expand our understanding of the Moon’s composition, surface processes, and potential for future resource utilization. One of its key payloads, the Chandrayaan-2 Large Area Soft X-ray Spectrometer (CLASS), was designed to perform X-ray fluorescence (XRF) spectroscopy to determine the elemental composition of the lunar surface with unprecedented accuracy.

This report focuses on the analysis of extensive data collected by the CLASS instrument, highlighting the processes and methodologies employed to determine elemental abundances. Using advanced spectral analysis tools like XSPEC, these elemental abundances were mapped onto the lunar albedo map to explore surface correlations. Furthermore, to address the challenges posed by the instrument’s native spatial resolution, this work leverages machine learning techniques to achieve a resolution enhancement to 2 km. The insights gained from this study not only enhance our understanding of lunar surface heterogeneity but also lay the groundwork for future advancements in planetary remote sensing and data analysis.

II. PRELIMINARIES

A. Solar Flares and its use in Lunar Elemental Analysis

A solar flare is a burst of energy from the Sun, which creates high-energy X-rays that are crucial for the study of the elemental composition of the Moon. Through these X-rays striking the lunar surface, stimulating atoms to emit characteristic signals, we can identify and map elements on the Moon.

Class	Intensity Range (W/m ²)
Class A	$< 10^{-7}$
Class B	$10^{-7} - 10^{-6}$
Class C	$10^{-6} - 10^{-5}$
Class M	$10^{-5} - 10^{-4}$
Class X	$> 10^{-4}$

TABLE I: Classification based on intensity range

1) *Formation of Solar Flares:* In the Sun’s corona, magnetic field lines may twist and tangle due to the convective and rotational motion within the Sun, leading to an increase in magnetic energy in certain areas. When the tension in these lines reaches a critical threshold, the field lines snap and reconnect, releasing the stored energy as electromagnetic radiation, high-energy particles, and thermal energy. This energy heats the surrounding plasma to millions of kelvin, accelerates particles to high speeds, and produces intense radiation, particularly in X-ray and ultraviolet (UV) bands [1]–[4].

2) *Solar Flare Classification:* The Geostationary Operational Environmental Satellite (GOES) program classifies solar flares based on their X-ray intensity within the 0.1–0.8 nm wavelength range. The classification includes five classes—A, B, C, M, and X—each representing a tenfold increase in X-ray flux intensity measured in watts per square meter at Earth’s distance from the Sun. Each class is further divided on a linear scale from 1 to 9. For instance, an X5 flare is five times stronger than an X1 flare, and X-class flares are the most powerful, followed by M, C, B, and A classes [5], [6].

3) *Appropriate Flare Classes for XRF Data Acquisition:* Solar flares provide X-ray energy to excitation elements on the lunar surface. The flare class is crucial for XRF spectroscopy in determining which elements can be excited and detected.

- **C, M, and Low X-Class Flares:** These have sufficient X-ray intensity to produce fluorescence emissions from various elements on the lunar surface, including Mg, Al, Si, Ca, and Fe. They balance event energy and spectral range, exciting the necessary elements without saturating the detectors and minimizing signal interference from high solar irradiance [7].
- **A, B, and High X-Class Flares:** A and B-class flares lack the energy needed for significant XRF signals, especially for heavier elements like Ca and Fe. High X-class flares (e.g., >X5) produce intense X-rays that can saturate

detectors, introduce noise, and distort XRF signals for lighter elements due to sudden intensity changes. Furthermore, there are inconsistencies in XRF data from high X-class flared due to their flux fluctuations [8], [9].

B. Atomic Interactions Involving X-rays from Solar Flares on the Lunar Surface

The Moon has no atmosphere and no magnetic field; therefore, the effects of solar radiation happen directly on the surface. These interactions of X-rays from solar flares with the surface encompass complex atomic and physical processes that can alter the composition of the Lunar regolith and provide valuable data for remote sensing. These interactions can generally be described by the following: photoelectric effect, X-ray fluorescence (XRF), scattering processes, and Auger electron emissions.

1) Photoelectric Effect and X-ray Fluorescence (XRF):

The photoelectric effect is the main atomic interaction that causes the production of X-ray fluorescence (XRF) when high-energy X-rays from solar flares collide with atoms in the lunar regolith. In this process, an incident photon ejects an electron from one of the inner shells of an atom, usually the K or L shells, leaving behind a vacancy. The energy of the incoming photon must overcome the binding energy of the electron in the shell, and this is expressed through the following equation:

$$h\nu = E_{\text{binding}} + E_{\text{kinetic}} \quad (1)$$

where $h\nu$ is the energy of the incident photon, E_{binding} is the electron's binding energy, and E_{kinetic} is the kinetic energy of the ejected electron.

Immediately following the ejection of an inner-shell electron, the atom undergoes a sequence of electronic transitions to stabilize itself. An electron from the higher energy shell, for instance, an L or M shell electron will fall to occupy the gap in the inner shell, typically the K shell, leaving excess energy to be carried out as an X-ray photon. The photon's energy is equivalent to the energy gap between the shells and is specific for the atom considered, for this reason, referred to as characteristic XRF line [10].

For instance, if the K shell of a magnesium atom is ionized, an electron from the L shell will fall to fill this vacancy, but it will emit a photon with an energy of the order of 1.25 keV. This is the characteristic $K\alpha$ line for Mg. If the displacement is a jump from a higher shell, say, M to K, the resulting $K\beta$ line is generally at a little higher energy than the $K\alpha$ line [11], [13].

2) *The Auger Effect: A Competing Process to XRF:* Sometimes, instead of emitting an X-ray due to electron transition, another electron from the atom, known as an Auger electron, may be ejected. This is the Auger effect, which favors lighter elements (generally atoms with atomic numbers less than 20). In many cases, Auger emission probability may be higher than that of XRF [10].

While the Auger effect reduces the number of X-ray photons produced by certain elements, it does not significantly effect

heavier elements like Si, Ca and Fe, where XRF is more likely to occur and is the dominant de-excitation mechanism

3) *Scattering Processes: Rayleigh and Compton Scattering:* In addition to the photoelectric effect and Auger emission, scattering plays an important role in determining the behavior of X-rays on the lunar surface. The dominant mechanisms are Rayleigh (coherent) and Compton (incoherent), both depending on the energy of the X-rays and the physical properties of the regolith. Such scattering processes dominate the redistribution of radiation and measured XRF intensities.

- **Rayleigh Scattering:** Rayleigh scattering is a coherent process that involves the interaction where photons are scattered without any energy loss, meaning they retain the same energy as the incident photons. This occurs because the interaction takes place with the bound electrons of atoms, and during this scattering event, there is negligible energy transfer. The scattered radiation remains in phase with the incident radiation, which is characteristic of coherent scattering. This scattering mechanism dominates when the incident photon interacts with particles much smaller than its wavelength.

- **Total Rayleigh Scattering cross section (σ_{Rayleigh}):** Rayleigh scattering cross-section as a function of scattering angle (θ) is given by:

$$\sigma_{\text{Rayleigh}}(\theta) = \frac{8\pi}{3} \left(\frac{r_e}{\lambda} \right)^4 \left(\frac{1 + \cos^2 \theta}{\sin^4 \theta} \right) \quad (2)$$

Where:

- * r_e is the classical electron radius ($r_e \approx 2.818 \times 10^{-15}$ m),
- * λ is the wavelength of the incident radiation,
- * θ is the scattering angle, and
- * The factor $\frac{1 + \cos^2 \theta}{\sin^4 \theta}$ arises due to the angular dependence of the scattering.

And the total Rayleigh scattering cross-section is given by:

$$\sigma_{\text{Rayleigh}} = \int_0^\pi \sigma_{\text{Rayleigh}}(\theta) d\Omega \quad (3)$$

where $d\Omega$ is the differential solid angle, which in spherical coordinates is:

$$d\Omega = \sin \theta d\theta d\phi \quad (4)$$

[15]

- **Compton Scattering:** Compton scattering is an incoherent process in which the incident photon transfers part of its energy to the electron, causing the photon to lose energy and scatter in a new direction. The scattered photon no longer maintains a phase relationship with the incident photon due to the energy transfer and the random nature of the scattering event. This scattering mechanism dominates the interaction of high-energy photons, such as X-rays and gamma rays, with matter.

- **Total Compton Scattering cross section** (σ_{Compton}): The total Compton scattering cross-section for an X-ray photon interacting with an electron can be described by the Klein-Nishina formula [16], which gives the differential cross-section:

$$\frac{d\sigma}{d\Omega} = \frac{r_e^2}{2} \left(\frac{E'}{E} \right)^2 \left(\frac{E}{E'} + \frac{E'}{E} - \sin^2 \theta \right) \quad (5)$$

Where:

- * r_e is the classical electron radius,
- * E is the energy of the incident photon,
- * E' is the energy of the scattered photon,
- * θ is the scattering angle, and
- * $\frac{E'}{E} = \frac{1}{1 + \frac{E}{m_e c^2} (1 - \cos \theta)}$, where m_e is the mass of the electron and c is the speed of light.

The total Compton scattering cross-section is obtained by integrating the differential cross-section over all solid angles:

$$\sigma_{\text{Compton}} = \int \frac{d\sigma}{d\Omega} d\Omega \quad (6)$$

This gives the total cross-section for scattering, which is primarily governed by the electron density in the material (in this case, the lunar regolith).

4) Influence of Photoelectric Cross-Sections and Fluorescence Yields on XRF Efficiency:

- **Photoelectric Cross-Section:** This is the likelihood that an X-ray photon is going to knock out an electron from a given shell. Generally, it increases with a higher atomic number and decreases with increased photon energies. Elements having a larger atomic number have high cross-sections, which means they tend to become more likely to undergo photoelectric effect that tends to result in XRF emissions [10].
- **Fluorescence Yield:** The fluorescence yield is the probability that a vacancy in a given shell will lead to the emission of an X-ray rather than an Auger electron. The fluorescence yield increases with atomic number; therefore, heavier elements are more likely to emit XRF photons, whereas lighter elements are likely to predominantly emit Auger electrons rather than X-rays. Such a yield is especially critical for the interpretation of the XRF signal since elements having higher yields show stronger fluorescence lines [26].

C. XRF Lines and Data Analysis

The photons of X-rays that are emitted due to transitions have specific energy levels for each emitting element, resulting in a characteristic XRF line spectrum for each element.

1) *Characteristic XRF Lines:* XRF lines fall into broad categories based on their source:

- **K α Lines:** These are the strongest and most frequently observed lines in XRF research. They are caused due to transitions from the L shell to the K shell.

- **K β Lines:** These are generally weaker than K α lines and generally occur at higher energies as transitions from the M to the K shell result in these lines.
- **L α and L β Lines:** Transitions involving L and M shells are possible and may also be observed but these can only be generally seen in XRF spectra from heavier elements [10], [11].

2) *Matrix Effects: Absorption and Secondary Fluorescence:* The XRF spectra obtained from the lunar surface are not only influenced by the primary fluorescence of individual elements but also by inter-elemental interactions, commonly known as matrix effects. These effects involve absorption and enhancement effects.

- **Self-Absorption:** When an X-ray photon emitted from an atom interacts with surrounding atoms in the sample, it may be absorbed by the material surrounding it before it can be emitted off the surface and into the detector. The self-absorption effect weakens the strength of the XRF line recorded for elements that have weaker-energy emissions [10].
- **Enhancement Effect (Secondary Fluorescence):** In secondary fluorescence, primary XRF emission from one element excites the nearby atoms. For example, K-shell X-rays from calcium can cause L-shell fluorescence of adjacent iron atoms that enhance the Fe XRF line intensity. This secondary fluorescence effect, though it assists in strengthening the signal, makes the interpretation of XRF data difficult and needs to be corrected in quantitative analysis [7], [17].

3) *Surface Texture, Grain Size, and Solar Variability:*

- **Surface Roughness and Particle Size:** The rough and granular characteristics of the Lunar regolith have a bearing on the intensities of the XRF. The rough surface scatters more and secondary fluorescence is enhanced due to smaller particles as reported by Maruyama et al. [17] and Narendranath et al. [7].
- **Solar X-ray Variability:** Solar X-ray intensities, particularly during flares, show much variability which influences the XRF signal. Solar X-ray flux is continuously monitored and measured by Chandrayaan-2 with its Solar X-ray Monitor (XSM) to ensure the accurate calibration of XRF data, accounting for the variability due to the Sun (Pillai et al., 2021).

4) *Spectral Analysis and Interpretation of XRF Data:* XRF spectra from the CLASS instrument contain discrete emission peaks that correspond to specific elements, superimposed on a continuous background signal from scattered solar X-rays, cosmic rays, and instrumental noise. Spectral analysis, including corrections for matrix effects and solar variability, is performed with software packages like XSPEC and PyXSPEC to derive elemental abundances accurately [7], [12].

D. Theoretical Modeling

Theoretical modeling allowed for a better understanding of the XRF data by accurately accounting for the complex

interaction between X-rays and the material. By incorporating factors such as the scattered continuum, mass attenuation coefficients, and fluorescent X-ray intensity, the model considers the influences of the sample's composition and geometry, as well as the incident X-ray energy. This modeling was done as described below.

1) *Fluorescent X-Ray Intensity*: The total fluorescent X-ray intensity is modelled as summation of primary fluorescent x-ray intensity ($I_1(ip)$) and secondary fluorescent x-ray intensity ($I_2(ip)$) [26]. Where ($I_1(ip)$) and ($I_2(ip)$) are given by,

$$I_1(ip) = \frac{1}{\sin \Psi} \int_{\lambda_m}^{\lambda_i} \frac{Q_{ip}(\lambda) I_0(\lambda)}{\frac{\mu(\lambda)}{\rho} / \sin \Phi + \frac{\mu(ip)}{\rho} / \sin \Psi} d\lambda \quad (7)$$

$$I_2(ip) = \frac{1}{2 \sin \Psi} \sum_{jq} \int_{\lambda_m}^{\lambda_i} \frac{Q_{jq}(\lambda) Q_{ip}(jq) I_0(\lambda)}{\frac{\mu(\lambda)}{\rho} / \sin \Phi + \frac{\mu(ip)}{\rho} / \sin \Psi} d\lambda \times \left\{ \frac{\sin \Psi}{\frac{\mu(ip)}{\rho}} \log \left(1 + \frac{\frac{\mu(ip)}{\rho} / \sin \Psi}{\frac{\mu(jq)}{\rho}} \right) + \frac{\sin \Phi}{\frac{\mu(\lambda)}{\rho}} \log \left(1 + \frac{\frac{\mu(\lambda)}{\rho} / \sin \Phi}{\frac{\mu(jq)}{\rho}} \right) \right\} \quad (8)$$

Emission probability of the fluorescent x-rays, p-line of the element i, ($Q_{ip}(\lambda)$) is given by

$$Q_{ip}(\lambda) = \frac{\mu_i(\lambda)}{\rho_i} W_i K_i \omega_i R_p^i \quad (9)$$

$$Q_{ip}(jq) = \frac{\mu_i(jq)}{\rho_i} W_i \omega_i R_p^i K_i \quad (10)$$

and other terms in the expression are in the table

2) *Total Mass Attenuation Coefficient*: The mass attenuation coefficient (μ/ρ) represents the extent to which a material attenuates (reduces the intensity of) radiation per unit mass. This property is intrinsic to the material and reflects how radiation, such as X-rays or gamma rays, is absorbed and scattered as it travels through the substance. It is a quantification of material's ability to interact with and weaken the radiation.

For a composite material (μ/ρ) in units of (cm^2/g) it is given by a weighted average with weights W_j single elements as $(\frac{\mu}{\rho})_i$ [18]

$$\frac{\mu}{\rho} = \sum_j W_j \left(\frac{\mu}{\rho} \right)_j \quad (11)$$

where

$$\sum_j W_j = 1 \quad (12)$$

3) *Scatter Continuum*: The total scattering cross section (σ_{total}) is Defined as summation of scattering cross sections due to Rayleigh scattering (σ_{Rayleigh}) and Crompton Scattering (σ_{Crompton})

$$\sigma_{\text{total}} = \sigma_{\text{Rayleigh}} + \sigma_{\text{Crompton}} \quad (13)$$

where the value of total Rayleigh (elastic) scattering cross-section ($\sigma_{\text{Rayleigh}} = \sigma_R$) is given by [25]:

$$\sigma_R = \frac{r_0^2}{2} \int_{\theta_{\min}}^{\theta_{\max}} (1 + \cos^2 \theta) |F(x, Z)|^2 2\pi \sin \theta d\theta \quad (14)$$

Where:

- σ_R is the elastic scattering cross section,
- $F(x, Z)$ is the atomic form factor,
- r_0 is the radius of electron, and
- θ is the scattering angle

and the intensity of elastically scattered spectrum (I_R) from an infinitely thick sample can be computed by

$$I_R = \int \frac{I_0(E) \sigma_R(E)}{\mu(E) [\text{cosec } \phi + \text{cosec } (\psi)]} dE \quad (15)$$

Where:

- ϕ is the incident angle,
- ψ is the emission angle,
- E is Energy,
- $\sigma_R(E)$ is the elastic scattering cross section as a function of energy, and
- $\mu(E)$ is the linear attenuation coefficient as a function of energy

E. Instrumentation

1) *CLASS*: CLASS instrument onboard Chandrayaan-2 is designed to perform XRF spectroscopy, which enables the detailed measurement of elemental abundances across the lunar surface. CLASS consists of 16 Swept Charge Devices (SCDs) arranged in four quadrants, each containing four SCDs. The detectors operate in the 0.8–15 keV range, targeting major rock-forming elements such as magnesium (Mg), aluminum (Al), silicon (Si), calcium (Ca), titanium (Ti), and iron (Fe) [9], [21]. CLASS's passive collimator achieves a field of view of 12.5 km × 12.5 km from an altitude of 100 km, providing the high spatial resolution necessary for detailed lunar mapping [7]. The SCDs maintain optimal spectral resolution at a nominal temperature of -20°C without requiring active cooling systems, and the large geometrical area of 64 cm² gives CLASS greater sensitivity and spatial coverage than previous lunar spectrometers [21].

2) *Solar X-ray Monitor (XSM)*: The X-ray Solar Monitor (XSM) complements CLASS by recording the incident solar X-ray spectrum in real-time. The XSM data is essential, as the XRF signals from lunar elements are dependent on the intensity of the incoming solar X-rays, which vary with solar activity [9]. Using a Silicon Drift Detector (SDD), XSM records the solar X-rays in the 1–15 keV range with a spectral

Notation	Description
ϕ	The angle made by the incident beam with the sample surface.
ψ	The angle made by the emergent beam with the sample surface.
$I_0(\lambda)$	The intensity of x-ray of wavelength λ .
$I(ip)$	The intensity of the x-ray of p -line emitted from element i , where i refers to the element and p refers to the spectral line.
$\mu(\lambda)$	The linear absorption coefficient of the specimen for the x-ray of wavelength λ .
$\mu(ip)$	The linear absorption coefficient of the specimen for the characteristic x-ray, p -line of the element i .
$\mu_j(\lambda)$	The linear absorption coefficient of the element j for the x-ray of wavelength λ .
$\mu_j(ip)$	The linear absorption coefficient of element j for the characteristic x-ray, p -line of element i .
ρ	The density of the specimen.
ρ_i	The density of element i .
W_i	The weight fraction of element i in the specimen.
ω_i	Fluorescent yield of element i .
R_p^i	The intensity fraction of the ip -line in the characteristic x-ray series which ip -line belongs to.
K_i	The absorption jump of element i .
λ_m	The minimum wavelength of exciting fluorescent radiation.
λ_e	The wavelength of the absorption edge of element i .

TABLE II: Notations used in equations

resolution of 180 eV at 5.9 keV, producing data every second. These XSM readings enable calibration of the CLASS data, allowing for adjustments to account for fluctuations in solar intensity and ensuring accurate elemental measurements [20], [21].

In cases where XSM data is unavailable because the Sun is outside its field of view, GOES (Geostationary Operational Environmental Satellite) solar flux data is used as an alternative. The GOES data allows for the estimation of solar coronal temperature, from which a solar spectrum is generated using CHIANTI spectral models. While this method provides a viable substitute, some systematic uncertainties remain, particularly for elements like iron (Fe) and silicon (Si), due to the differences in spectral line intensities during solar flares [7].

F. Data Collection and Calibration of CLASS Swept Charge Devices (SCDs)

1) *XRF Data Acquisition*: CLASS operates continuously on the sunlit side of the Moon. Here, solar X-rays interact with atoms on the lunar surface, causing these atoms to emit secondary X-rays that are characteristic of each element. By recording the energy and intensity of these emissions, CLASS captures elemental signatures that represent the abundance of specific elements across the lunar surface [7].

2) *Solar Spectrum Calibration*: Simultaneously, XSM records the solar spectrum, which is used to calibrate the XRF measurements obtained by CLASS. This calibration step is critical for compensating for the variations in solar intensity that directly impact the strength of lunar XRF signals. Accurate elemental analysis relies on this calibration to produce reliable measurements of lunar elemental abundances [9], [21].

3) *Background Radiation Collection*: During lunar night periods, CLASS collects background radiation data to account for non-solar sources of radiation, such as galactic cosmic rays. This background data is subtracted from the XRF measurements to ensure that the detected signals primarily reflect the elemental composition of the lunar surface rather than external noise [20].

Data from CLASS and XSM is processed and archived in ISRO's PRADAN repository, following the Planetary Data System (PDS) format, making it accessible for ongoing analysis by the scientific community [21], [23]. The integration of CLASS and XSM on Chandrayaan-2 marks a significant advancement in lunar elemental analysis, providing valuable elemental maps that enrich our understanding of the Moon's composition and geological history.

4) *Channel-to-Energy Calibration*: Calibrating these channels to specific photon energies is essential for precise data analysis. Calibration is performed using a JSC-1A lunar simulant under controlled conditions with a silver anode X-ray tube to account for the temperature dependencies of the detectors. Both pre-launch and in-flight recalibrations are conducted to ensure accuracy, following protocols detailed in the CLASS User Manual [22].

5) *Spectral Redistribution Function (SRF)*: A Monte Carlo-based charge transport model, initially developed for the Chandrayaan-1 CLASS instrument, is used to create the Spectral Redistribution Function (SRF) for CLASS. The SRF models the redistribution of incident photon energies across different detector channels, correcting for detector response characteristics. This function is crucial for accurate spectral analysis, accounting for channel-specific energy variations.

6) *Blocking Fraction and Transmission*: The CLASS system includes filters and collimators to manage the incoming X-rays, partially blocking specific photon paths. This blocking fraction is measured pre-launch and during in-flight adjustments to ensure an accurate assessment of the effective X-ray photon flux reaching the detector. This quantification is essential for modeling the detector's effective area and maintaining calibration accuracy [23].

G. Instrument Response Files: RMF and ARF

The Redistribution Matrix File (RMF) and Ancillary Response File (ARF) are critical components in processing and interpreting CLASS XRF data.

- **RMF (Redistribution Matrix File)**:

The RMF file characterizes the relationship between detected photon energies and their corresponding incident

energies, accounting for detector effects and spectral redistribution. It is essential for translating raw channel counts into calibrated energy values [47].

- ARF (Ancillary Response File):

The ARF file defines the effective area of the detector at different energy levels, enabling the quantification of photon fluxes. Together with the RMF, the ARF allows for accurately determining elemental abundances by adjusting for energy-dependent variations in detector sensitivity. This effective area, $A_{eff}(E)$, is given by [9]:

$$A_{eff}(E) = A_{geom} \times 16(1 - F)X(E)\epsilon(E)$$

where A_{geom} is active geometric area of each SCD, F is the collimator blocking fraction, X is the X-Ray transmission through the Al filter and ϵ is the detection efficiency, both a function of energy.

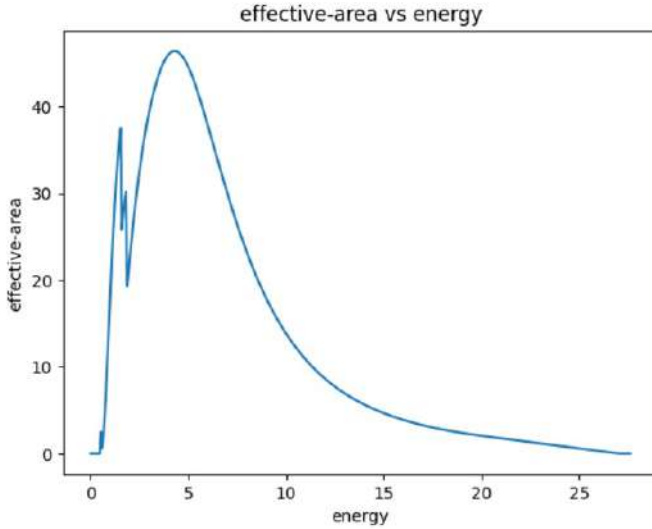


Fig. 1: Effective Area vs Energy graph

III. ALGORITHM

A. Data

CLASS is operated continuously on the lit side of the moon to record the XRF photons excited by the lunar surface when the solar flares hit the surface of the moon. While night side observations (5 min) every orbit are used to measure the background in the lunar orbit. CLASS instrument is designed to detect this X-ray emission in the 0.8-15 keV energy range. Since it is important to identify the spectrum solar flare-produced Xrays that trigger the generation of XRF lines, a companion payload on Chandrayaan-2, the X-ray solar monitor (XSM) observes the sun simultaneously to measure solar flares X-ray spectrum. These XRF spectrum are composed of a scattered continuum and X-ray fluorescence lines along with a background continuum that is taken to be steady over many months.

The lunar surface is constantly exposed to Galactic Cosmic Rays (GCRs), solar wind, and occasional Solar Energetic

Particles (SEPs), ranging from a few keV to GeV. Low-energy particles deposit energy in SCDs as a continuum, while high-energy particles pass through. CLASS efficiently distinguishes particle events (spanning hundreds of pixels) from X-ray events (limited to 2–3 pixels). Counts above ≈ 7 keV predominantly arise from particles, with notable X-ray peaks, such as Cu (8.05 keV) and the Al filter (1.47 keV).

The 7–16 keV light curve over nine months shows monthly background enhancements due to geotail passage. Sunlit spectra contain XRF lines (e.g., O-K α , Mg, Al, Si), while night-side observations reveal background variations. The background spectra for XRF analysis are selected based on low levels of particle flux and remain stable over months.

The spectral analysis involves several key steps. First, the background spectrum appropriate for the observation, $B(E)$. $B(E)$, is constructed. Next, the incident solar X-ray spectrum corresponding to CLASS observations $I_0(E)$, is derived using XSM data. This is followed by determining the scattered spectrum of the solar flare reflected from the lunar surface $I_R(E)$. From the spectral analysis, X-ray line fluxes of various elements are extracted. Finally, these XRF line fluxes are converted into elemental abundances using the x2abundance model. Background emission comes from cosmic X-rays, secondary particles, and X-rays produced by high-energy particles interacting with the instrument. Energetic particles can also leave partial signals in the detector, copying X-ray-like patterns. The changing particle environment causes variations in the background, which must be accurately understood in order to analyze the XRF line fluxes.

The Moon experiences two main particle environments in a lunar month:

- 1) Solar Wind and Cosmic Rays (≈ 24 Days): Steady background caused by solar wind and cosmic rays with energies from keV to GeV.
- 2) Earth's Geotail (≈ 6 Days): Background affected by energetic electrons (1–several keV) as the Moon passes through the geotail near the full moon phase.

Sudden particle bursts from solar events can cause sharp increases in CLASS counts, unrelated to solar X-rays, leading to temporary changes in the background.

B. Solar Spectrum

The incident solar spectra $I_0(E)$ for the observed CLASS timings were derived from XSM data, providing key inputs for the analysis of lunar XRF spectra. Spectral analysis was carried out using the XSMDAS software developed by ISRO. This software allowed us to create the appropriate spectrum files for 96-second intervals corresponding to the XRF spectrum being analyzed more easily, using the *xsmgenspec* command.

The fitting of solar spectra was performed in XSPEC on the energy from 1.2 to 7.2 KeV interval using vapec with an additional powerlaw component as the model, with initial parameters set to coronal abundances based on Feldman [50]. This approach ensures a robust representation of the observed solar X-ray intensity. Other models, such as using only vapec

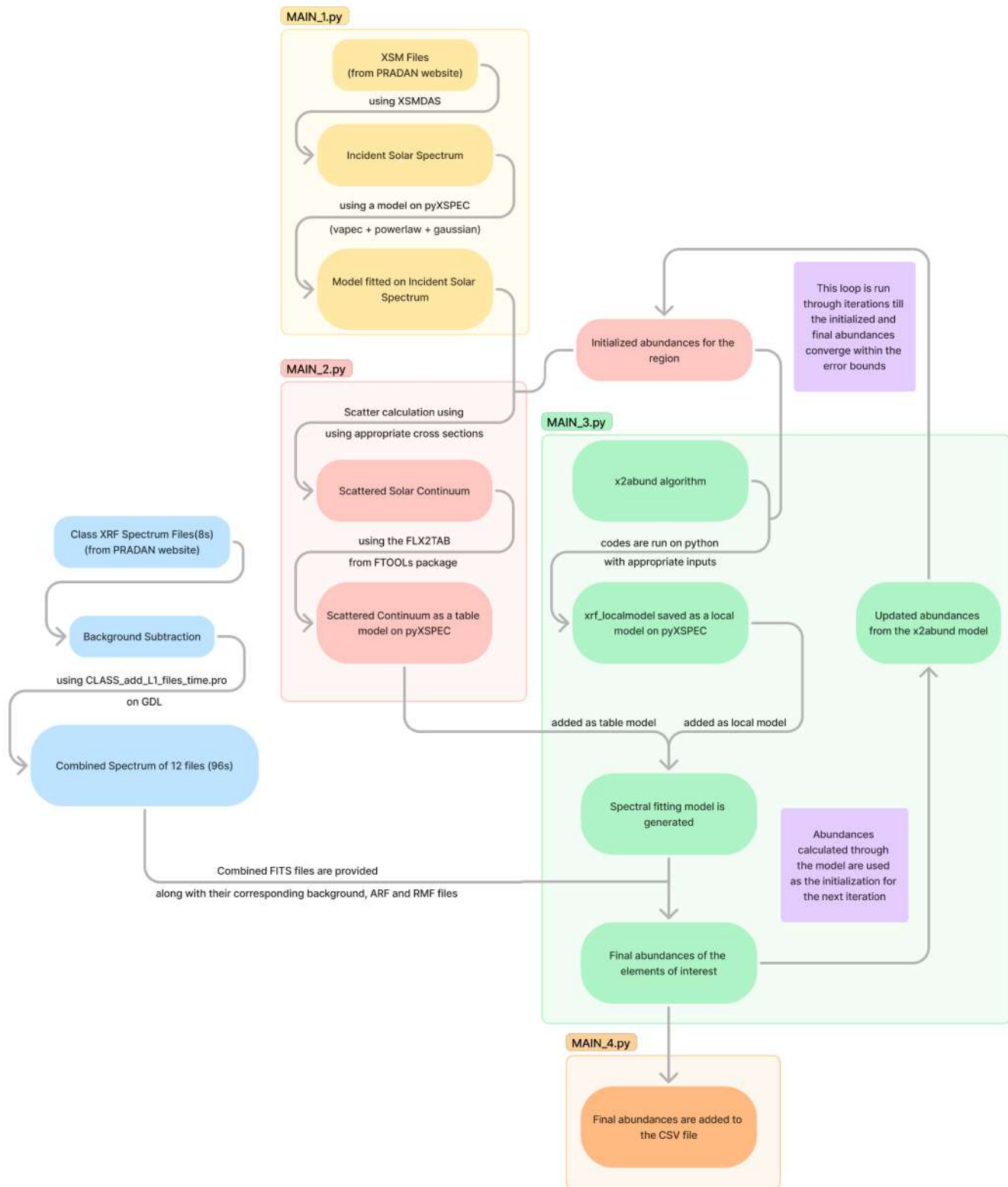


Fig. 2: Flowchart of the algorithm used for deriving elemental abundances from XRF spectra.

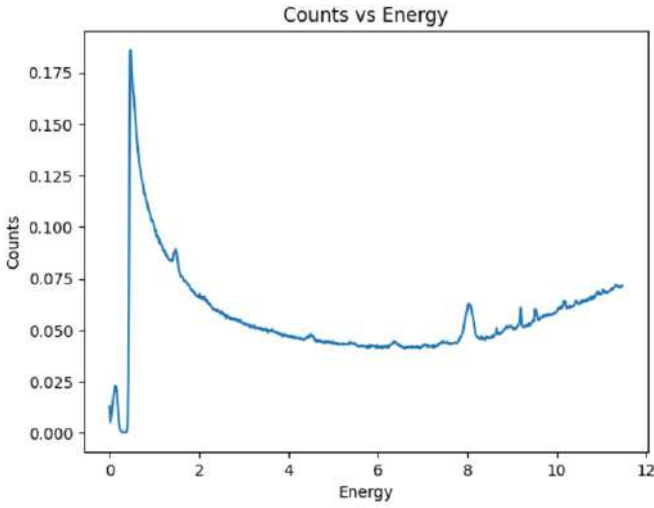


Fig. 3: Intensity of background radiation

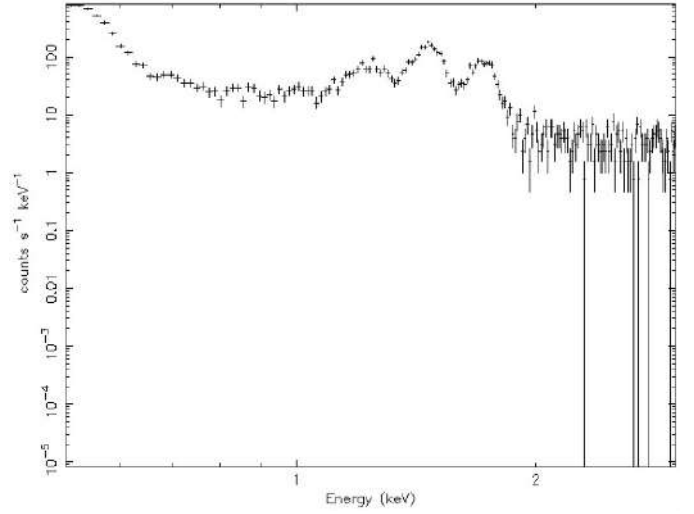


Fig. 5: Combined XRF Spectrum Data plotted against Energy on XSPEC

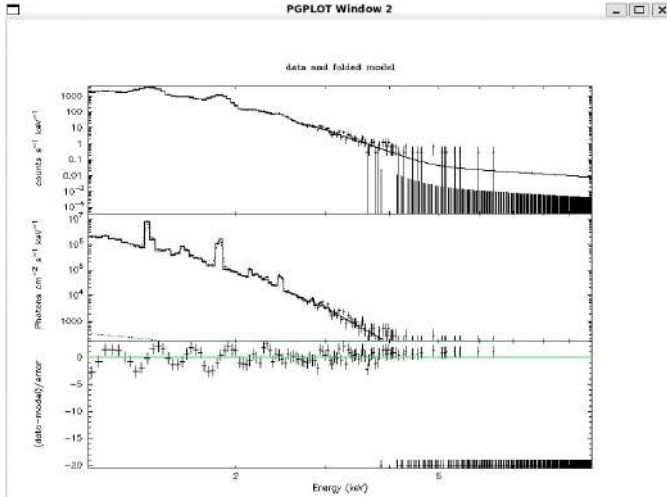


Fig. 4: Solar spectrum data fitted with the Solar Continuum model

or vvapec, were also tested but resulted in similar or worse fits.

The solar spectral model obtained from this fitting process was then used in *x2abundance*. This model was essential for computing the lunar XRF line intensities, which are critical for determining elemental abundances on the lunar surface. Additionally, the scattered component of solar X-rays, reflected from the lunar surface, was calculated using the derived solar spectrum model, ensuring accurate interpretation of the lunar XRF data.

C. Calculation of Scatter Continuum ($I_R(E)$)

We used XSM data to obtain the solar spectrum and spacecraft telemetry for the observing angles. Starting with an apriori composition based on the lunar highland and mare regions, we iteratively modeled the scattered component.

We adopted the feldspathic terrane composition from Korablev et al. [2003] [49] for the apriori model. The scattered spectrum was then used as a component in spectral fitting to derive XRF line fluxes. The determined abundances were used in further iterations to refine the scattered spectrum, which was incorporated into the spectral fitting process. Convergence was generally achieved within two iterations, with line fluxes stabilizing within error bounds.

We used the FFAST dataset derived from the NIST database to find the $\frac{\mu}{\rho}$ values and the $\frac{\sigma}{\rho}$ values corresponding to each element.

Weighted sum of $\frac{\sigma}{\rho}$ values using all elements is determined to calculate the equivalent $\frac{\sigma}{\rho}$ values and similarly a weighted sum of $\frac{\mu}{\rho}$ values are determined to calculate the equivalent $\frac{\mu}{\rho}$ values for a given energy bin. Finally, we calculate the scatter continuum corresponding to each energy bin, generating the scatter continuum from the solar continuum.

This scatter continuum is a function of the $\frac{\mu}{\rho}$ values and $\frac{\sigma}{\rho}$ values corresponding to the elements on the surface of the moon which majorly include Fe, Ti, Ca, Na, O, Mg, Al, Si. The values we have used are included in the following table to calculate the scatter continuum. These are the major elements found on the surface of the moon and are also detected by xray spectroscopy and thus these elements are considered.

Scatter continuum also depends on the weight fractions that are mentioned in 11. These weight fractions correspond to the abundances of particular elements on the surface of the moon.

D. *x2abundance*

We now describe the formulation of the XRF inversion algorithm, *X2Abundance*, which converts the observed XRF line intensities into elemental abundances. The algorithm employs analytical expressions based on the Fundamental Parameters (FP) method, assuming a thick, homogeneous, and flat sample. The expressions by Shiraiwa and Fujino [1966] [26], outlined

in 7 and 8 are utilized to compute XRF line intensities from the sample. The key steps in x2abundance for determining elemental abundances are outlined below, with the sequence of execution of major steps summarized in Fig. 6.

Since the lunar surface's elemental composition is dominated by elements with XRF line energies in the range of 0.9–4.2 keV, the computation focuses on elements with K-shell atomic binding energies below 10 keV. Using fundamental atomic data, such as mass absorption coefficients and fluorescence yields, the code analytically calculates the XRF line intensities for a given matrix (M_j), incident spectrum ($I_0(E)$), and observational geometry.

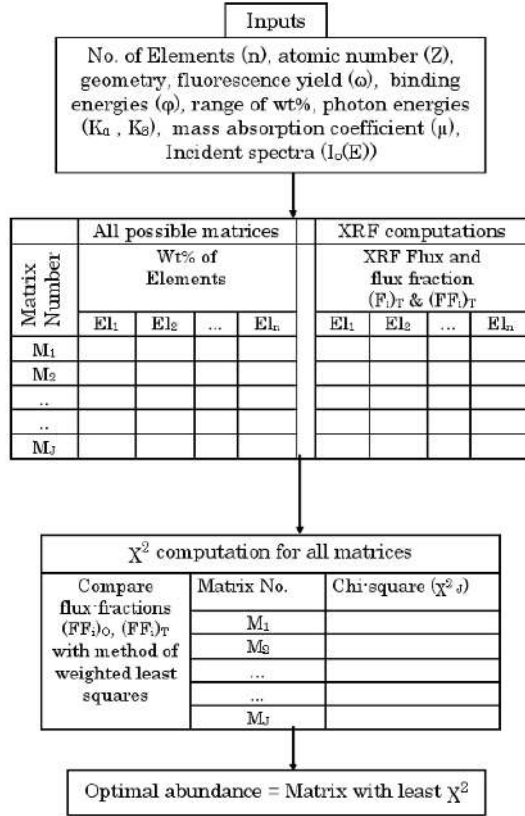


Fig. 6: Important steps involved in execution of x2abundance

Qualitative analysis of the XRF spectrum identifies the elements present in a sample. The set of elements and their corresponding weight fractions is referred to as the "matrix." Different combinations of weight fractions are generated for these elements, ensuring the total always sums to 1. For a given matrix M_j , the condition $\sum W_i = 1$ is maintained, where W_i represents the weight fraction of each element.

To optimize computations for samples with many elements, constraints based on prior knowledge can limit the range of weight fractions. For example, if an element's abundance is known to exceed 0.6 in a sample containing four elements, its weight fraction is restricted to the range 0.6–0.99. The remaining three elements collectively vary between 0.01 and 0.4, significantly reducing the number of possible combinations.

The program calculates the line flux (F_i) and flux fraction (FF_i) for each element in every matrix M_j .

Using the tools that have been discussed the methodology that we used to finally find the abundance corresponding to a single 96 seconds XRF spectrum fits file combined in a sliding window fashion has been discussed below. We explored various approaches to combine the 8s XRF spectrum FITS files provided by the CLASS instrument, which are available for download from the Pradan website. Three primary strategies were considered: the sliding window approach, the running check approach, and a combined approach (sliding + running). These methods are described below:

1) Sliding Window Approach:

The sliding window approach involves combining adjacent FITS files in a sequential manner. For example, files 1-12 are combined together, then files 2-13, and so on. This approach ensures significant overlap between adjacent tracks, which is crucial as the satellite moves across different positions. This method optimizes the spatial coverage by ensuring smooth transitions between tracks.

2) Running Check Approach:

In the running check approach, we sequentially combine files and perform spectral fitting using three Gaussian functions and a continuum. The goal is to minimize the chi-squared value of the fit, ideally between 0.8 and 2. Files are combined until a satisfactory fit is achieved, and once a set of files has been selected, the next combination starts from the next available file. This approach helps in reducing processing time, but it may come at the cost of lower accuracy, particularly when subpixel resolution is critical.

3) Combined Approach (Sliding + Running):

The third approach merges the sliding window and running check approaches. Initially, files are combined using the sliding window method until a combination of three Gaussian functions and a continuum provides an optimal fit. Once a satisfactory fit is identified, the process continues with the next set of files, starting from the second file of the previous set. Although this approach incorporates the benefits of both previous methods, it did not lead to significant improvements in the fitting results and thus was not implemented for our final analysis.

The sliding window approach was chosen for our analysis as it ensures sufficient overlap between tracks, which is crucial for capturing accurate spectral features, particularly given the motion of the satellite. Although it is more time-consuming, this approach is essential for achieving high subpixel resolution. The running check approach, while faster, sacrifices some accuracy in the subpixel resolution, which is a key factor for our study. The combined approach did not show substantial improvements and was not pursued further. Further research can explore alternative strategies for combining FITS files to optimize processing time while maintaining the accuracy needed for high-resolution analysis.

The time interval of 96s was taken and the XSM spectrum file which are available on a day wise basis. Now we find the solar spectrum for that interval of 96 seconds using the XSMDAS software by ISRO. Only those files were considered that belong to the time intervals which were a subset of the GTI and GOES solar flare data in which we included solar flares of class B,C,M because A is a low intensity solar flare and is not enough for characteristic x-ray peaks to be differentiable from noise. X class solar flares were rejected because the instrument does not generate reliable data in these solar flares. The standard GTI include all times when the unocculted Sun is within the full FOV ($\pm 38^\circ$) of XSM and also with the instrument health parameters within recommended ranges.

Now we use the discussion above for calculation of the scattered continuum from the spectrum using 15 Once the scattered continuum is determined. The scattered continuum is stored as a table model in XSPEC and a xrf_localmodel derived from the NIST database and input abundances is used to calculate the XRF line component of the XRF spectrum. We used PyXspec(Python interface to xspec) for all the purposes. To derive the abundances we assumed an initial abundance that was a weighted sum of the fraction of area under highland regions and area under mare regions multiplied by the corresponding average abundances in those regions for every element. Initialization using data from [48] and validated from [49] gave us good results. The background-subtracted XRF spectrum is fit using the scattered continuum and XRF lines with abundances as parameters for training. The inversion algorithm is used for training and fitting the abundance parameters. We also experimented with the number of iterations required to calculate the abundances, scattered continuum, and XRF line intensities. We found that one iteration was enough to obtain a low margin of error in the abundance values. Although performing two iterations was ideal, three iterations led to overfitting and overcomputation. We continued this process and analyzed files corresponding to approximately 75 days. We optimized our code And the results obtained have been discussed in the following section.

IV. SUBPIXEL RESOLUTION

The task of sub-pixel resolution using overlapping tracks is modeled as semi-supervised deep spatial interpolation using a sparse dataset. This problem is approached using a hybrid architecture, consisting of a Graph Neural Network (GNN) and a Convolutional Neural Network (CNN), to capture local and global relationships inherent in the elemental abundance distribution. The discussion of the use of overlapping tracks for subpixel resolution and ultimately arriving at a $2\text{km} \times 2\text{km}$ resolution map has been discussed in the following three subsections. Subsection A focuses on the introduction and problem formulation, it also talks about the difficulties in learning the mapping function. Subsection B covers the theoretical perspective of the implementation covering the theory behind the three-part methodology in detail. Subsection C focuses on the experimentation and the results obtained.

A. Introduction and Problem Formulation

A specific point s on the lunar surface is defined by its 2D coordinate value $(\text{lat}_s, \text{lon}_s) \in \mathcal{S}$, where \mathcal{S} represents the entire (latitude, longitude) space, i.e.

$$\mathcal{S} = [90^\circ, -90^\circ] \times [-180^\circ, 180^\circ].$$

Each location s is associated with two components $\mathbf{x}_s, \mathbf{y}_s$ belonging to \mathcal{X}, \mathcal{Y} . \mathcal{X} denotes the input feature space that is designed to capture both the spatial characteristics such as latitude, longitude, and surface characteristics, and \mathcal{Y} represents the output space of elemental abundances.

The goal is to learn the predictive mapping function

$$: \mathcal{X} \rightarrow \mathcal{Y},$$

which captures the relationship between the input feature space \mathcal{X} and elemental abundances \mathcal{Y} , s.t.

$$(\mathbf{x}_s) = \mathbf{y}_s \quad \forall s \in \mathcal{S}.$$

Learning the exact mapping function is challenging due to spatial heterogeneity across the lunar surface. Formally, this variability due to spatial heterogeneity can be expressed as

$$(x_s) \neq (x_{s'})$$

for $s, s' \ni \|\mathbf{x}_s - \mathbf{x}_{s'}\|_2 > \epsilon$ for some $\epsilon > 0$. This task of learning is further complicated by the sparsity and large spatial span of elemental abundances calculated from XRF spectrum.

Thus we try to model this problem of finding as a non-convex optimization problem, and try to approximate from a hypothesis class \mathcal{H} that is rich enough to capture both the local variations while maintaining consistency in the elemental distribution across the global domain. We hypothesize that a deep hybrid model composed of a Graph Neural Network (GNN) and a Convolutional Neural Network (CNN) can approximate this \mathcal{H} because of their abilities to capture both large scale spatial relationships as well as localized patterns. Specifically, the GNN is adept at modelling non-Euclidean spatial dependencies between different regions, while the CNN can identify local patterns within individual regions. The hybrid model can thus effectively account for the spatial heterogeneity and sparsity inherent in the problem.

Any such approximate function \mathfrak{R} over any spatial region \mathfrak{R} , must account for variations in spatial features and surface characteristics throughout \mathfrak{R} . Thus instead of having a single over the entire \mathcal{S} , which would have led to an under-constrained, highly non-convex optimisation problem, we partitioned the lunar surface into 64 equisized segments. This allows us to give a more precise and better region-specific approximation of \mathfrak{R} for each of these regions. The models can predict elemental abundances at high resolution across the entire lunar surface by learning these adaptive relationships.

Thus, we can formulate our problem as follows: our objective is to predict elemental abundances at a finer spatial resolution of (approximately) $2\text{km} \times 2\text{km}$ using the abundances measured over larger regions provided by the CLASS instrument, i.e., given a set of N observed data samples $\{L_{1,i}, L_{2,i}, \mathbf{A}_i\}_{i=1}^N$,

where $L_{1,i} \in [90^\circ, -90^\circ]^4$, $L_{1,i} \in [-180^\circ, 180^\circ]^4$ are the latitude and longitudes of the 4 corner points of any observation, and $\mathbf{A}_i \in \mathbb{R}^8$ are the observed elemental abundances of the 8 elements ('Fe', 'Ti', 'Ca', 'Si', 'Al', 'Mg', 'Na', 'O') in that observation, we need to approximate the region specific mapping function \mathfrak{R} for all the regions. This region-specific learned mapping $\mathfrak{R} : \mathcal{X}_{\mathfrak{R}} \rightarrow \mathcal{Y}$, where $\mathcal{X}_{\mathfrak{R}}$ is the region constrained input feature space, should generalize to both seen locations (where information about elemental abundances is available) and unseen locations.

We solve this problem by breaking it into 3 steps:

- 1) Information Initialisation
- 2) Abundance Population
- 3) Abundance Generalization

In Step 1, we initialize and define various data structures and constructs to help with the remaining steps. In Step 2, i.e. Abundance Population, we map the processed data onto the data structures initialised above, and in Step 3, i.e. Abundance Generalization, we use the information at the known grid locations to approximate \mathfrak{R} and predict elemental abundances at all points in that region \mathfrak{R} . We also utilize overlapping tracks to increase the density of known data grid locations.

1) *Related works*: Recent advancements in Spatial interpolation and resolution enhancement highlight innovative methods that uses neural networks, attention mechanisms, and hybrid architectures to overcome limitations of traditional approaches. Viana and Barbosa [27] introduced an attention-based spatial interpolation technique to enhance house price prediction accuracy. Their method avoids reliance on costly data sources such as satellite imagery or census data. By combining a Euclidean-based attention mechanism for structural feature similarity with Geo Attention for geographic proximity, the model generates house embeddings that capture both structural and spatial contexts. Similarly, Zhou et al. [28] developed a frost prediction model tailored for agricultural applications that eliminates the need for on-site historical data or sensors. This model uses geographic and environmental factors, such as elevation, vegetation, and distance, to aggregate predictions through weighted averages. Appleby et al. [29] extended Kriging principles by integrating them with Graph Neural Networks (GNNs) to create Kriging Convolutional Networks (KCN). In this innovative approach, data points are modeled as graph nodes, with edge weights representing spatial proximity. By utilizing attention mechanisms, the KCN dynamically adjusts the influence of neighboring nodes, offering significant flexibility and avoiding retraining for new datasets.

In the domain of X-ray fluorescence (XRF) imaging, super-resolution has been employed, particularly in Earth-based applications. For instance, methods such as "Deep Learning Enhanced Super-Resolution XRF Microscopy" [30] and "XRF Image Super-Resolution Using Dictionary Learning" [31] employ high-resolution structural or RGB data to complement low-resolution XRF measurements. Other approaches, like "Super-Resolution for Macro XRF Data Collected from Old Master Paintings" [32] and "Resolution-Enhanced XRF Microscopy via Deep Learning" [33], utilize multimodal data

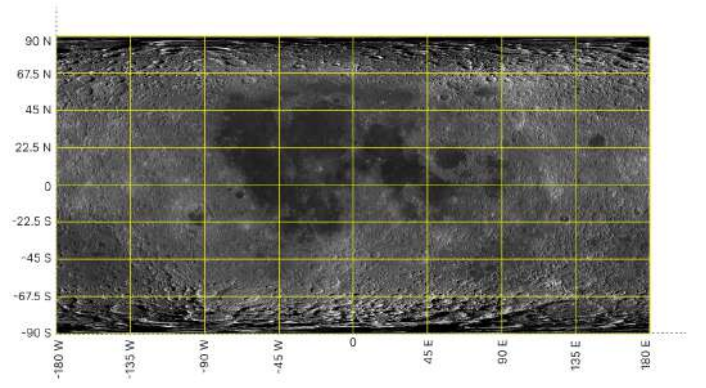


Fig. 7: Partitioning of the Lunar Surface in 64 divisions

fusion with complementary imaging modalities such as ptychography or RGB images to achieve resolution enhancement. These strategies have proven effective in controlled environments, such as laboratory settings and artwork analysis.

However, such methods face challenges when applied to lunar XRF data due to unique constraints, including extreme data sparsity, spatial heterogeneity, and the absence of high-resolution complementary imaging. To address these challenges, our methodology employs a hybrid architecture combining Graph Neural Networks [27] and Convolutional Neural Networks [38]. Our methodology exclusively relies on lunar XRF data, effectively overcoming the limitations of external dependencies.

B. Proposed Methodology

The entire lunar surface is divided into 64 equisized regions based on latitude, and longitude. Each region has a latitude span of 22.5° and longitude span of 45° . This can be visualised in Figure 7. We construct a Global Information Bank (*GIB*) to store all computation information, defined as follows:

$$GIB = \bigcup_{(i,j) \in [1\dots 8]^2} (GIB_{i,j}),$$

where $GIB_{i,j}$ is the region specific *GIB*, defined as,

$$GIB_{i,j} = (L_1, L_2, \mathfrak{A}, \mathfrak{W}, \mathfrak{M}),$$

where L_1 is the vector of latitudes of center of super-resolved pixels and L_2 is the vector of longitudes, \mathfrak{A} is the matrix of elemental abundances at every pixel, \mathfrak{W} is a matrix of surface characteristics vector \mathbf{W}_k of every pixel k , and \mathfrak{M} is a 2 class vector, which is either 1 or 2, signifying if the center of the pixel lies in a Mare region or a Highland region on the lunar surface.

The final hybrid model aims to learn the mapping from $\mathfrak{W}, \mathfrak{M}, L_1, L_2$ to \mathfrak{A} for known points, and tries to generalize this mapping to unknown points by using the similarity between the surface characteristics (or \mathbf{W}_k 's) and the spatial distance as captured by L_1 and L_2 . The GNN tries to incorporate global

context by considering pixels that are spatially far but feature-wise close, while the CNN tries to incorporate local context and patterns from spatially close nodes.

The complete methodology for achieving sub-pixel resolution consists of 3 main steps:

1) *GIB Initialization*: For each of the 64 regions, we initialize $GIB_{i,j}$ by finding the centers of each of the superresolved pixels. Each $22.5^\circ \times 45^\circ$ region is divided into a 342×682 grid, s.t. the latitude or longitude difference between any 2 super-resolved pixels corresponds to approximately 2 km at the equator.

For each super-resolved pixel's, k , latitude and longitude, we calculate \mathbf{W}_k , to denote its surface characteristics. To ensure feature continuity and overlap between 2 adjacent pixels, instead of taking a $2\text{km} \times 2\text{km}$ surface region, we consider a $12.5\text{km} \times 12.5\text{km}$ surface region centered at that pixel and calculate its surface characteristics by employing a ResNet50 model [35]. The model outputs surface characteristic vectors of length 2048. To speed up computation, we selected the top 300 features greedily based on relevance and redundancy using the Max-Relevance Min-Redundancy (mRMR) feature selection method. This method greedily selects the feature that is the most informative (quantified by maximum variance), while minimizing overlap (correlation) with already selected features [45]. This 300 length vector \mathbf{W}_k forms the surface characteristic vector at super-resolved pixel k .

2) *Abundance Population*: The processed elemental abundances, given by, $\{L_{1,i}, L_{2,i}, \mathbf{A}_i\}_{i=1}^N$, represents a data region of size approximately equal to $12.5\text{km} \times 100\text{km}$. In order to map these abundances into the *GIB*, we make the following assumptions:

- The $12.5\text{km} \times 100\text{km}$ region is composed of 8 adjacent $12.5\text{km} \times 12.5\text{km}$ regions, each of which contribute equally to the final abundance calculated over the entire $12.5\text{km} \times 100\text{km}$ region.
- The abundance of each of the $12.5\text{km} \times 12.5\text{km}$ region is assumed to be concentrated at its center coordinate.

These 2 assumptions allow us to map every $12.5\text{km} \times 100\text{km}$ observation onto 8 different points in the *GIB*. We made these assumptions to balance maximum population and ability to deviate from the observed data.

In order to find the transformation vector $B \in \mathbb{R}^{1 \times 8}$, s.t. the calculated $12.5\text{km} \times 12.5\text{km}$ abundances C_i for each $i = [1 \dots 8]$, can best approximate the abundance over the entire $12.5\text{km} \times 100\text{km}$ region $A \in \mathbb{R}^{8 \times 1}$, we phrase and solve a Lagrangian optimization problem.

Define a matrix $C \in \mathbb{R}^{8 \times 8}$, whose columns are given by

$$C_i = A \cdot b_i$$

, where b_i is the i -th element of the transformation row vector $B \in \mathbb{R}^{1 \times 8}$, $A \in \mathbb{R}^{8 \times 1}$ are the abundances of the 8 elements over 1 data $12.5\text{km} \times 100\text{km}$ region, and the columns of the matrix $C \in \mathbb{R}^{8 \times 8}$ represents the elemental abundances of the 8 smaller parts. In order to get a constrained optimization problem, we make the following assumptions: The elemental assumptions

at each of the center pixels, of each of the $12.5\text{km} \times 12.5\text{km}$ do not deviate much from the expected elemental abundance at that location, assuming its either a Mare or Highland region.

This assumption gives rise to the following loss function:

$$\text{Loss}(B) = \sum_{i=1}^8 \|A \cdot b_i - \tilde{A}\|_2^2,$$

where $\tilde{A} \in \mathbb{R}^{8 \times 1}$ either equals to A_h or A_m , which represents the average elemental abundances of Highland and Mare respectively.

This loss function can be written as

$$\text{Loss}(B) = \|A \cdot B - D\|_F^2,$$

where $\|\cdot\|_F$ represents the Frobenius norm of the matrix, and $D \in \mathbb{R}^{8 \times 8}$ is a matrix such that its i -th column $D_i = \tilde{A}$.

The first set of assumptions also leads to the following global consistency constraint:

$$\frac{1}{8} \sum_{i=1}^8 C_i = A,$$

which can be rewritten as:

$$\frac{1}{8} A \cdot (B \cdot \mathbf{1}_8) = A,$$

where $\mathbf{1}_8$ is an 8×1 column vector of ones.

In addition to the global consistency constraint, we impose the non-negativity constraint on the elemental abundances. The elemental abundances for the i -th location, $C_i = [c_{i,1}, c_{i,2}, \dots, c_{i,8}]^T$, must satisfy:

$$c_{i,j} \geq 0, \quad \text{for } j = 1, 2, \dots, 8.$$

Thus the optimization problem subject to the constraints mentioned above can be formulated as:

$$\min_B \|A \cdot B - D\|_F^2,$$

To solve this constrained optimization problem, we introduce two Lagrange multipliers λ & μ . Hence the Lagrangian function for the optimization problem becomes

$$L(B, \lambda, \mu) = \|A \cdot B - D\|_F^2 + \lambda^T (A \cdot (B \cdot \mathbf{1}_8) - 8A) + \mu^T \cdot \max(0, -B).$$

Here μ is the Lagrange multiplier for the non-negativity constraint, and $\max(0, -B)$ introduces a penalty for negative values in B .

To solve the optimization problem with the added non-negativity constraint, we take the gradients [46] of the Lagrangian with respect to B , λ , and μ :

$$\frac{\partial L}{\partial B} = 2A^T (A \cdot B - D) + \lambda^T A + \mu^T \cdot \text{sign}(-B),$$

$$\frac{\partial L}{\partial \lambda} = A \cdot (B \cdot \mathbf{1}_8) - 8A,$$

$$\frac{\partial L}{\partial \mu} = \max(0, -B).$$

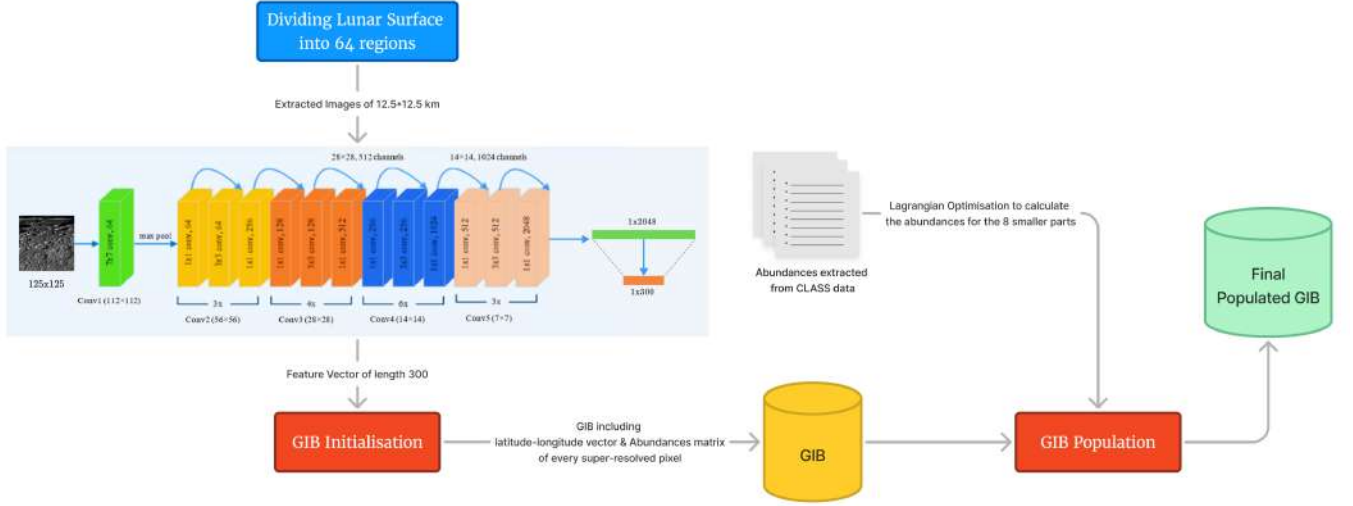


Fig. 8: GIB initialisation with latitude longitude and the abundances vector along with the top 300 features extracted using the ResNet50 network to obtain the initialised GIB. Further populating them with the elemental abundances using Optimisation to obtain the final populated GIB .

Setting the gradients to zero, we solve for B , λ , and μ :

$$2A^T (A \cdot B - D) + \lambda^T A + \mu^T \cdot \text{sign}(-B) = 0,$$

$$A \cdot (B \cdot \mathbf{1}_8) - 8A = 0,$$

$$\max(0, -B) = 0.$$

We solve the optimization problem iteratively by updating B , λ , and μ using gradient descent:

$$B_{\text{new}} = B_{\text{old}} - \eta \frac{\partial L}{\partial B},$$

$$\lambda_{\text{new}} = \lambda_{\text{old}} - \eta \frac{\partial L}{\partial \lambda},$$

$$\mu_{\text{new}} = \mu_{\text{old}} - \eta \frac{\partial L}{\partial \mu},$$

where η is the learning rate.

This optimization problem is solved for all $\{L_{1,i}, L_{2,i}, \mathbf{A}_i\}_{i=1}^N$ and the columns of the calculated matrix C gives the elemental abundances at the 8 $12.5\text{km} \times 12.5\text{km}$ region's center super-resolved pixel, which is updated in the *GIB*.

3) *Abundance Generalization*: Abundance generalization consists of learning the mapping $\mathfrak{R} : \mathcal{X}_{\mathfrak{R}} \rightarrow \mathcal{Y}$ for each of the 64 well-define regions \mathfrak{R} . We learn this mapping using the sparsely populated *GIB* created in Step 2.

To capture long-range relationships we employ a Graph Neural Network. To represent our lunar region as a graph, we consider each super-resolved pixel as a Node [44]. Since each lunar region consists of $(342 \times 682 =) 233244$ such nodes, it would be infeasible to load the entire region as a single graph. It is required to break a single region spanning $22.5^\circ \times 45^\circ$, into multiple subregions, each of which will have a subgraph. To ensure easier learning of the mapping

function on this region, the subgraphs have to be overlapping, otherwise, it would be impossible to go from global minimum of 1 subregion to the global minimum of another subregion. This requirement of overlapping subregions also has the benefit of Data Diffusion, i.e. once the elemental abundances are predicted for 1 subregion, this allows for that new information to propagate to all overlapping subregions. Such a data diffusion is extremely important considering the sparsity of the data.

We divide each region consisting of 342×682 super-resolved pixels into 78 subregions, by taking each subregion to have 100 pixel length and 100 pixel breadth and a stride of 50 pixels in each direction, thus giving us 6 grid cells along the latitude and 13 grid cells along the longitude. Let $\mathcal{H} = \{H_1, H_2, \dots, H_{78}\}$ represent the set of these overlapping graphs where each graph H_k corresponds to a subregion within a region in the 8×8 grid and overlaps with its adjacent subregions.

For each region \mathfrak{R} we construct H_l for $l = [1..78]$, the overlapping subgraph's of that region. Each $H_l = (\mathcal{N}_l, \mathcal{E}_l)$, since we construct the overlapping subgraph with a fixed size, $|\mathcal{N}_l| = 100 \times 100 = 10,000 \forall l \in [1..78]$. Each node $n \in \mathcal{N}_l$ contains the following information:

- $\text{lat}_n, \text{lon}_n$: The latitude and longitude of the center of the super-resolved pixel that node n represents.
- \mathbf{W}_n : A column vector of length 300 denoting the surface characteristics of the $12.5\text{km} \times 12.5\text{km}$ centered at the center of super-resolved pixel that node n represents.
- \mathbf{A}_n : A column vector of length 8 representing the Elemental abundances of the 8 elements if known at that node n , otherwise 0.

Since we want to capture long range dependencies and relationships in this graph, the set of edges in the graph must connect nodes even if they are spatially far but close

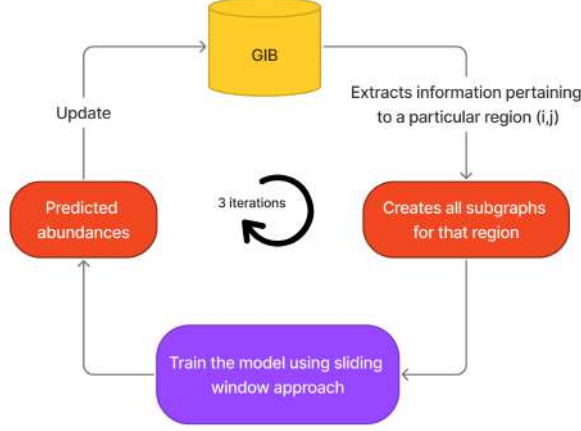


Fig. 9: Model pipeline for abundance generalisation. Pictorial representation that illustrates our workflow starting from extraction of information from GIB all the way to training the sub-graphs and updating the predicted abundances into the csv files.

w.r.t. surface characteristics. Thus we define an edge-weight function

$$w : (\mathcal{N}_1 \times \mathcal{N}_1) \rightarrow \mathbb{R}$$

as follows:

$$w(n_1, n_2) = \exp \left(-\alpha \cdot \text{haversine}(G_{n_1}, G_{n_2}) - \beta \cdot \|\mathbf{W}_{n_1} - \mathbf{W}_{n_2}\|_2^2 \right)$$

such that the scaling factor $\beta > \alpha$ implying the requirement that surface feature similarity matters more than spatial similarity. Here, G_{n_1} and G_{n_2} represents the latitude and longitude at each of n_1 and n_2 respectively. Thus, connections between nodes are determined by an edge weight function that decreases exponentially with spatial distance and feature-based dissimilarities. Here,

- $\text{haversine}(G_i, G_j)$ is the haversine distance between the geographic coordinates of nodes i and j [39].

$$\text{haversine}(G_i, G_j) = 2r \arcsin \left(\sin^2 \left(\frac{\text{lat}_j - \text{lat}_i}{2} \right) + \cos(\text{lat}_i) \cos(\text{lat}_j) \sin^2 \left(\frac{\text{long}_j - \text{long}_i}{2} \right) \right)^{1/2}$$

where r is the radius of the moon.

- $\|\mathbf{W}_i - \mathbf{W}_j\|_2^2$ is the squared Euclidean distance between the feature vectors of the nodes i and j .

For each node $n \in \mathcal{N}_i$, we select the top 100 neighbors with the largest edge weight, signifying their closeness either spatially or feature wise. The mapping function we aim to learn must account for both local and global relationships. We hypothesize that the following described hybrid model composed of GNN + CNN followed by a fusion deep layers

gives a rich enough Hypothesis class to approximate the mapping function. The complete model architecture has been shown in Figure 10.

The GNN component employs 2 GATv2Conv layers in succession. Each GATv2Conv layer computes node embeddings by dynamically attending to neighbors in a graph [37].

Let the input graph to any of the GATv2Conv layers be represented by a set of nodes \mathcal{N} and edges \mathcal{E} , with node features $\mathbf{X} \in \mathbb{R}^{|\mathcal{N}| \times F_{in}}$ and edge features $\mathbf{E} \in \mathbb{R}^{|\mathcal{E}| \times D}$. In our case, $F_{in} = 303$ (300 length surface characteristic vector, 1 scalar representing whether the super-resolved pixel that node n represents is either Mare or Highland, and 2 scalar values representing the latitude and longitude of that pixel). At any GATv2Conv layer, the updated representation of a node i is computed as:

$$\mathbf{h}'_i = \sum_{j \in \mathcal{N}(i) \cup \{i\}} \alpha_{ij} \mathbf{h}_j,$$

- \mathbf{h}'_i is the updated feature vector of node i .
- α_{ij} represents the attention coefficient between nodes i and j , defined as:

$$z_{ij} = \mathbf{a}^\top \text{LeakyReLU}(\mathbf{W}_s \mathbf{h}_i + \mathbf{W}_t \mathbf{h}_j + \mathbf{W}_e \mathbf{e}_{ij}),$$

$$\alpha_{ij} = \frac{\exp(z_{ij})}{\sum_{k \in \mathcal{N}(i) \cup \{i\}} \exp(z_{ik})}.$$

- $\mathbf{W}_s, \mathbf{W}_t, \mathbf{W}_e$ are learnable weight matrices for query nodes, key nodes, and edge features, respectively.
- \mathbf{a} is a learnable vector that computes attention scores.

The proposed GNN network allows conditioning the attention coefficients on the query node, this allows for learning richer node representations, compared to older methods based on static attention.

The CNN component processes spatial data represented as a grid, where node features are mapped to pixels using latitude (lat) and longitude (lon) indices. The mapping is computed as:

$$\text{lat_index}_i = \left\lfloor \frac{\text{lat}_i - \text{lat}_{\max}}{\text{lat}_{\min} - \text{lat}_{\max}} \cdot (n_{\text{grid}} - 1) \right\rfloor,$$

$$\text{lon_index}_i = \left\lfloor \frac{\text{lon}_i - \text{lon}_{\min}}{\text{lon}_{\max} - \text{lon}_{\min}} \cdot (n_{\text{grid}} - 1) \right\rfloor,$$

where n_{grid} is the number of grid points along each dimension. This grid structure is then passed through the CNN layers to get a final grid of extracted features. The CNN extracted features for each node are then extracted from the grid based on the indexing equations mentioned above.

The CNN comprises three of convolutional layers interspersed with max-pooling operations. Each convolution is defined as:

$$F_{ij}^{(l)} = \sigma \left(\sum_{p=-k}^k \sum_{q=-k}^k w_{pq}^{(l)} F_{i+p, j+q}^{(l-1)} + b^{(l)} \right),$$

where:

- $F_{ij}^{(l)}$ is the output at pixel (i, j) in layer l .
- $w_{pq}^{(l)}$ are the filter weights.
- $b^{(l)}$ is the bias term.

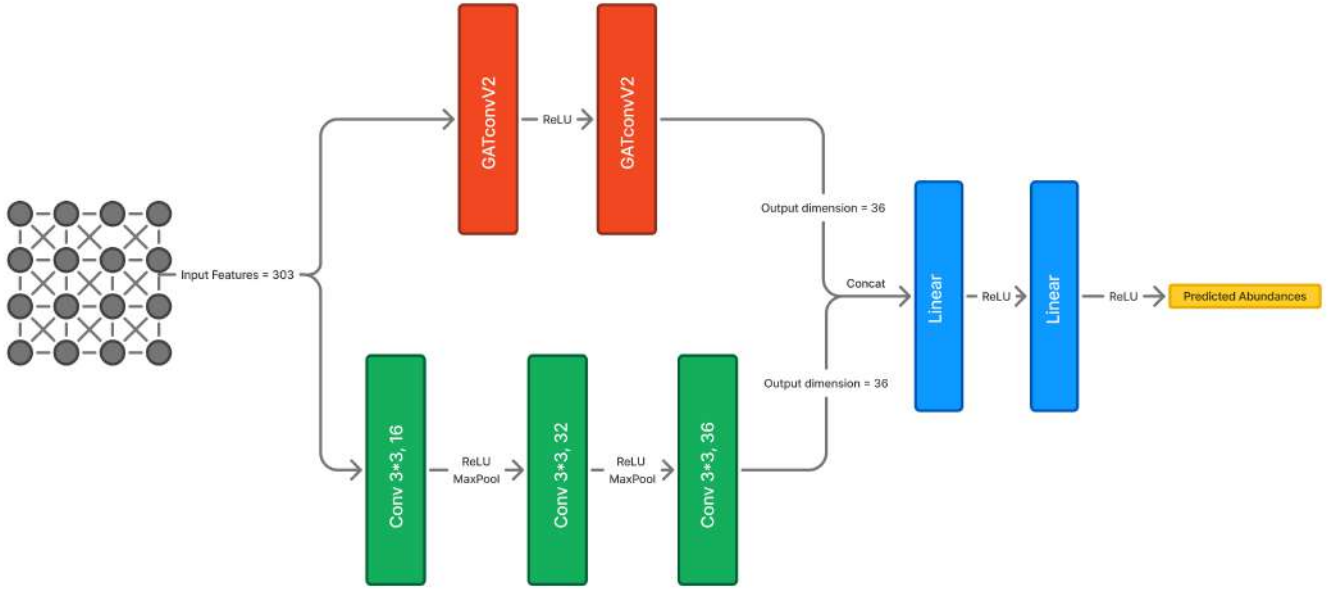


Fig. 10: The Hybrid Model architecture involving two GNN (GATv2conv) layers and three convolutional layers. The results of both the networks are concatenated and passed through fusion layers to obtain the final predicted elemental abundances.

- σ is the activation function (ReLU used here).
- k is half the size of the filter used in each dimension.

Forwarding a subregion through the GNN and CNN backbones results in node embeddings that encompass both the global context and local context for each node. These high dimensional embeddings can then be used to predict the elemental abundances by learning a mapping via deep neural network layers.

So, the outputs from the GNN and CNN are concatenated to form a unified representation:

$$\mathbf{h}_{\text{fusion}} = \text{ReLU}(\mathbf{W}_f[\mathbf{h}_{\text{GNN}}, \mathbf{h}_{\text{CNN}}] + \mathbf{b}_f),$$

where:

- $[\mathbf{h}_{\text{GNN}}, \mathbf{h}_{\text{CNN}}]$ is the concatenation of GNN and CNN outputs.
- \mathbf{W}_f and \mathbf{b}_f are the learnable weights and bias of the fusion layer.

The final prediction is computed using a fully connected layer:

$$\mathbf{y} = \mathbf{W}_o \mathbf{h}_{\text{fusion}} + \mathbf{b}_o,$$

where \mathbf{W}_o and \mathbf{b}_o map the fused representation to the output space of elemental abundances. This entire procedure has been illustrated in Figure 9.

Finding the correct mapping function/hypothesis in this expansive hypothesis class \mathcal{H} requires us to select a loss function that incorporates all the constraints inherent in the problem. These losses can be expressed as follows:

Weighted Masked Mean Squared Error (MSE) Loss: A weighted masked MSE loss is incorporated to enforce correct

predictions of abundances at known data points. Formally, it is defined as:

$$\mathcal{L}_{\text{masked_mse}} = \frac{\sum_{i=1}^N \text{mask}_i \cdot \sum_{j=1}^8 w_j \cdot (\hat{y}_{i,j} - y_{i,j})^2}{\sum_{i=1}^N \text{mask}_i}$$

where mask_i is an indicator function specifying if the abundances for node i are entirely known, w_j represents element-specific weights, and $\hat{y}_{i,j}$ and $y_{i,j}$ denote predicted and true abundances, respectively. This loss ensures the model focuses on accurate predictions for available data.

Weighted masked Logarithmic Loss: To address the wide dynamic range in elemental abundances, a logarithmic loss is added [34]. It emphasizes relative differences rather than absolute magnitudes, which is more indicative in case of elements with small abundance. The loss function is given by:

$$\mathcal{L}_{\log} = \frac{\sum_{i=1}^N \text{mask}_i \sum_{j=1}^8 w_j (\log(\hat{y}_{i,j} + \epsilon) - \log(y_{i,j} + \epsilon))^2}{\sum_{i=1}^N \text{mask}_i}$$

where ϵ is a small constant added for numerical stability, and the rest of the variables are as described above. This log loss allows every element to have an equal contribution in the loss.

Feature Similarity Loss: The Feature Similarity Loss is used to enforce consistency in elemental abundances prediction for nodes with similar surface characteristics. For a given subgraph H_t This loss is defined as:

$$\mathcal{L}_{\text{feature_sim}} = \frac{1}{|\mathcal{E}_t|} \sum_{(s,t) \in \mathcal{E}_t} w_{st} \cdot \|\hat{\mathbf{y}}_s - \hat{\mathbf{y}}_t\|_2^2$$

where $w_{st} = \exp(-\|\mathbf{W}_s - \mathbf{W}_t\|_2)$ is a weight reflecting the similarity between feature vectors \mathbf{W}_s and \mathbf{W}_t of nodes s

and t . By penalizing large abundance differences for nodes with similar features, this loss accounts for the alignment of predictions of nodes with known physical relationships.

Spatial Similarity Loss: The Spatial Similarity Loss enforces consistency in predictions between spatially close nodes. This constraint is based on the assumption that elemental abundances should vary smoothly. The loss is defined as:

$$\mathcal{L}_{\text{spatial_sim}} = \frac{1}{|\mathcal{E}_l|} \sum_{(s,t) \in \mathcal{E}_l} w_{st} \cdot \|\hat{y}_s - \hat{y}_t\|^2$$

with:

$$w_{st} = \exp\left(-\frac{\|\text{loc}_s - \text{loc}_t\|_2 - d_{\min}}{d_{\max} - d_{\min} + \varepsilon}\right)$$

where loc_s and loc_t are the spatial coordinates of nodes s and t , and d_{\min}, d_{\max} denote the minimum and maximum pairwise distances.

Deviation Loss: This loss enforces that the sum of predicted abundances is close to 100%. The deviation loss is given by:

$$\mathcal{L}_{\text{deviation}} = \frac{1}{N} \sum_{i=1}^N \left| \sum_{j=1}^8 \hat{y}_{i,j} - 100 \right|$$

The Weighted Masked MSE Loss and the Weighted Masked Logarithmic Loss are responsible for learning the mapping from node-level embeddings to predicted abundances for $2\text{km} \times 2\text{km}$ pixels where the data is already populated. The Feature Similarity Loss and Spatial Similarity Loss are responsible for smoothening the predicted abundances across nodes that are spatially and feature-wise close. These 2 loss functions are responsible for the generalization of the mapping function for nodes where abundances are not known.

All 5 of these loss functions guide the search process of the mapping function in the hypothesis class \mathcal{H} , to ultimately arrive at the best mapping function for that region.

The problem for finding the best mapping function in the hypothesis class \mathcal{H} involves optimization in a highly non-convex landscape. The non-convexity arises from the multiple non-convex loss functions, along with the non-convexity inherent in the model architecture. This makes the search for an optimal mapping function within the hypothesis class \mathcal{H} more challenging.

However, with empirical analysis we found that there does exist a global minimum basin, and thus the search problem can be formulated similar to a Spiked Matrix-Tensor model [43]. Thus using a learning rate scheduler that follows a search-convergence pattern, we can probabilistically guarantee convergence to the global minimum [43]. We used a Cosine Annealing Learning Rate scheduler, which follows a search-convergence pattern, along with various other heuristics, thus increasing our chances of convergence. The following methods were used to increase our chances of convergence:

Gradient Clipping was employed to prevent the issue of exploding gradients, which is common in regions of steep curvature in the loss landscape. For each parameter θ , the

gradient $\nabla\theta$ is rescaled when its norm exceeds a predefined threshold τ (1.0 in our case):

$$\nabla\theta \leftarrow \nabla\theta \cdot \min\left(1, \frac{\tau}{\|\nabla\theta\|_2}\right),$$

where $\|\nabla\theta\|_2$ is the L2 norm of the gradients. Imposing this constraint on the magnitude of the gradient can help prevent erratic training behaviour.

YOGI Optimizer is an adaptive gradient method, that is used to stabilize training in sparse and noisy gradient scenarios [40]. YOGI is different from traditional optimisers such as ADAM [42], since it introduces a corrective mechanism that adapts the second-moment estimate of the gradients v_t as follows:

$$v_t = v_{t-1} - \text{sign}(v_{t-1} - g_t^2) \cdot \eta,$$

where g_t is the gradient at time t and η is the learning rate. The parameter updates are given by:

$$\theta_{t+1} = \theta_t - \frac{\alpha}{\sqrt{v_t} + \varepsilon} \cdot g_t,$$

where α is the step size, and ε is a small constant for numerical stability. YOGI is very effective for non-convex optimization tasks because of its ability to adjust learning rates adaptively.

Cosine Annealing Learning Rate Scheduler was employed to adjust the learning rate during training in search-convergence fashion [41]. The learning rate η_t at step t is computed as:

$$\eta_t = \eta_{\min} + \frac{1}{2}(\eta_{\max} - \eta_{\min}) \left(1 + \cos\left(\frac{t}{T_{\max}} \cdot \pi\right)\right),$$

where η_{\min} and η_{\max} are the minimum and maximum learning rates, and T_{\max} is the total number of steps. The search-convergence exploration allows for effective navigation of this non-convex landscape.

A **Two-Phase Learning Scheme** was followed because of the presence of multiple loss functions. In the initial optimisation phase, the model was trained using only the weighted masked mean squared error ($\mathcal{L}_{\text{masked_mse}}$) and deviation loss ($\mathcal{L}_{\text{deviation}}$):

$$\mathcal{L}_1 = \mathcal{L}_{\text{masked_mse}} + \mathcal{L}_{\text{deviation}}.$$

This initial training allowed the model to find the global minimum of the convex MSE loss function and learn the mapping from features to abundances for known points. In the second phase of optimization, all the loss functions were used,

$$\mathcal{L}_2 = \mathcal{L}_{\text{masked_mse}} + \lambda_{\text{reg}} \cdot \mathcal{L}_{\log} + \mathcal{L}_{\text{feature_sim}} + \mathcal{L}_{\text{spatial_sim}} + \lambda_{\text{reg}} \cdot \mathcal{L}_{\text{deviation}}.$$

This phase focuses on generalizing the mapping from known nodes to unknown nodes.

C. Experimental Results and Conclusion

This section covers the experimental details, training details, mapping output and the dynamic nature of superresolution.

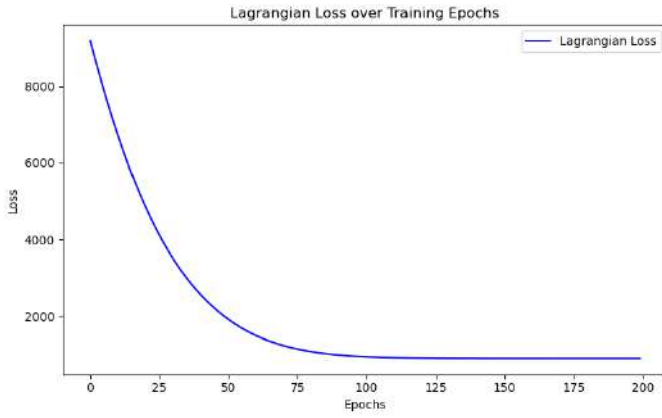


Fig. 11: Lagrangian minimization curve over epochs. This is calculated to distribute the abundances across 8 subregions of size 12.5 km x 12.5 km from abundances extracted from a region of size 12.5 km x 100 km.

1) *Abundance Population*: During the abundance population, we minimize the Lagrangian for 80 epochs with $\lambda = 1$ & $\mu = 2$. The minimization of the Lagrangian can be seen in Figure 11.

2) *Abundance Generalisation*: The model is trained for a region \mathcal{R} by iteratively generating all overlapping subgraphs from the *GIB* and then training the model on each of the subgraphs in a sliding window fashion, to ensure there is no sudden domain shift and the model can remain in the global minimum. This iteration happens 3 times to ensure proper data diffusion of the new samples.

Anytime new data comes, we update the *GIB* by calculating the new abundance by solving the Lagrangian for every new sample (Takes around 0.167 seconds for 80 epochs). Following this we update the *GIB* and retrain the model for the updated regions. Thus our model and proposed training algorithm is inherently dynamic.

3) *Mapping Output*: The mapped output for super-resolved Mg abundance in the Lunar Region $i = 0$ $j = 2$ which corresponds to the Lunar Region (90N,67.5N) and (90W,45W) has been shown in Figure 12

V. MAPPING AND VISUALIZATION

A. Introduction

Mapping and visualization are key techniques to understand the composition, evolutionary history, and the potential for future resource utilization of any geological terrain or structure. Our objective was to utilize data from the Chandrayaan-2 CLASS instrument to detect X-ray fluorescence (XRF) lines, which were then used to determine the elemental heterogeneity of the lunar surface and eventually plot the elemental abundance ratios of different elements detected on the lunar albedo map. We plotted two types of maps—heat maps and graduated maps—that showed the variation in the distribution of different elements on the lunar surface and helped us identify multiple locations rich in specific minerals. The data we gathered from

this endeavour could also be used to plan future missions and further develop our understanding of our only natural satellite.

B. Data Acquisition and Processing

The .fits files containing XRF spectral data from Chandrayaan-2 Large Area Soft X-ray Spectrometer (CLASS) for high solar flares intervals were taken. The spatial resolution for these files was 12.5 km by 12.5 km. These files went through thorough processing and fitting by the algorithm team to obtain data in the form of elemental abundancy with spatial coordinates of 12.5 km X 150 km resolution. The processed files were then given to ML team who in turn enhanced its sub-pixel resolution to 0.06 square degrees per pixel. The data format that we used was Comma-Separated Values (CSV). The CSV files directly processed from CLASS data as well as those with enhanced sub pixel resolution were further processed to make them suitable for use in the mapping software. Ratios between elements were also taken for better visualization. The final CSV thus obtained served as the input to the mapping software. Major Steps:

- 1) The CSV files obtained after fitting of XRF data were processed to add headers and then appended.
- 2) Further to make our heat and graduated maps, we needed to convert the input files from before and after sub pixel resolution enhancement in a specific format. For graduated maps, we converted latitude and longitude corresponding to each vertex (V0, V1, V2 and V3) in a row major format followed by elemental abundance and ratios.
- 3) For heat maps, we averaged out the coordinates of vertices to concentrate the abundances at just one point for each polygon followed by interpolation to handle the gap between two points.
- 4) This entire process was further automated by using python scripts so that new files could be dynamically added into the system with minimal manual intervention.

C. Tools Utilised

- 1) QGIS (Quantum Geographic Information System): For mapping the lunar surface, we used QGIS (Quantum Geographic Information System), an open-source GIS platform that is freely available and offers a range of features suitable for various types of geospatial data analysis and visualization. It has an extensive plugin ecosystem which could be leveraged for a variety of purposes such as spatial analysis, geoprocessing and even machine learning to some extent. Its cross-platform compatibility meant that all members of our team could use it even if they used different operating systems. It also supports a wide range if vector, raster and database formats. The fact that it is compatible with python (more on this later) and PostgreSQL also made it a good choice for us. Additionally, its open source nature meant that we could leverage its extensive community support for debugging purposes.

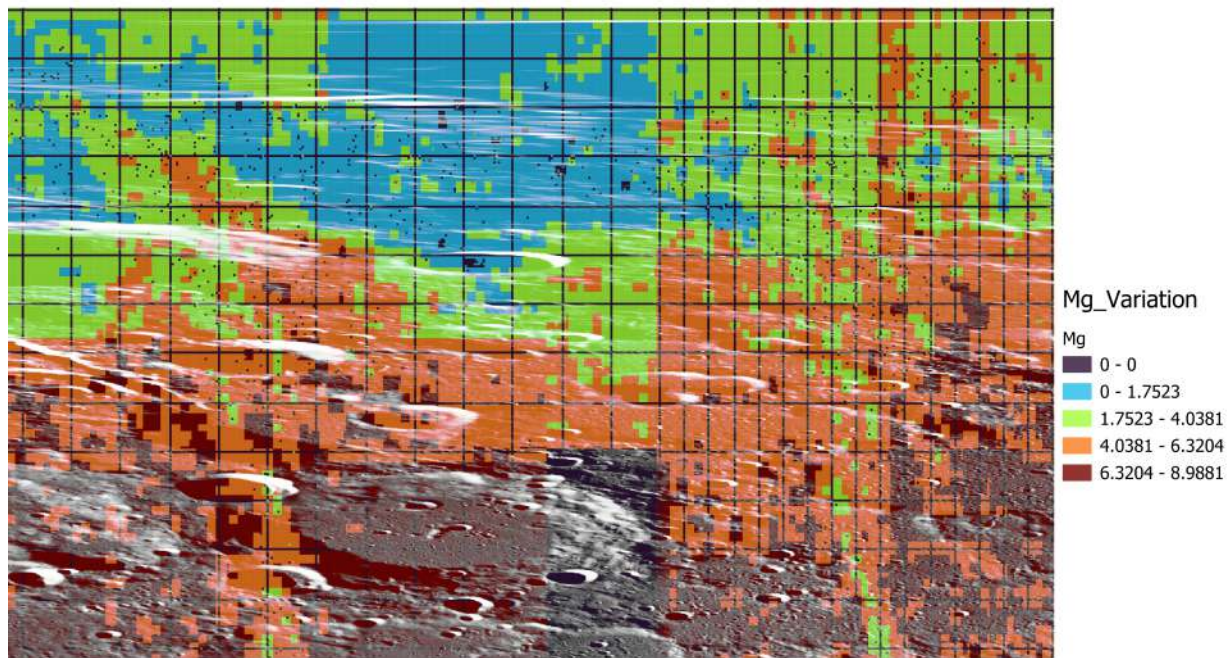


Fig. 12: Superresolved Mg Abundance in the lunar region (0, 2) corresponds to [(90N, 67.5N), (90W, 45W)]

- 2) **PyQGIS:** PyQGIS is a python library built to work with QGIS. It allows the user to interface with QGIS programmatically. QGIS has a built-in python console and text editor where source codes written in PyQGIS can be run locally. The primary use case of this library is to automate repetitive tasks such as creating and editing layers, performing spatial analysis, working with geospatial data, visualizing geographic information exporting etc. It also integrates quite well with other GIS tools.
- 3) **Web Mapping Services – Lunaserv :** Web Mapping Services (WMS) are standard protocols that allow users to request and display georeferenced maps over the internet. It provides easy access to geospatial data without the need for local storage, offering real-time updates and seamless integration with various GIS tools as long as there is a stable internet connection. For our purpose, we used Lunaserv, a specialized Web Mapping Service designed for planetary and lunar data with a special focus on educational and research purposes. It possesses a large catalogue of lunar maps of all types from standard LROC maps to oxide and mineral abundance maps. We have chosen the “luna_wac_global” map.
- 4) **GDAL (Geospatial Data Abstraction Library):** GDAL (Geospatial Data Abstraction Library) is an open-source library used for reading, writing, and transforming geospatial data formats. It provides robust tools for raster data manipulation, vector data processing and can also be connected with WMS.

D. Mapping Methodology

1) Importing Base Map

To obtain the lunar albedo map, we utilized the Lunaserv WMS provided by the Lunar Reconnaissance Orbiter Camera (LROC) team at Arizona State University. The data retrieval process involved the following steps:

- a) **Connecting to Lunaserv in QGIS:**
We connected Lunaserv as a WMS layer in QGIS by establishing a connection through the WMS URL: <http://webmap.lroc.asu.edu/>. This connection enabled us to access Lunaserv’s public layers directly within QGIS.
- b) **Layer Selection:**
We chose the “luna_wac_global” map (ID:170 Title: LROC WAC Global 100m/px) since it had the best resolution in that repository. For exporting this layer locally, we used GDAL on terminal.
- c) **CRS (Coordinate Reference System):**
The CRS (Coordinate Reference System) was chosen to be EPSG:4326, although it is usually defined for Earth’s map, Lunaserv’s maps also support this CRS.
- 2) **Uploading Data and Plotting**
CSV files with latitude and longitude coordinates along with their corresponding abundances obtained and processed from .fits files were imported as a layer in QGIS using Python scripts (PyQGIS). Polygons for each set of four coordinates (V0, V1, V2, V3) were plotted on the LROC WAC lunar albedo map to identify the regions where XRF (X-Ray Fluorescence) lines were detected.
- 3) **Generating Maps**
 - a) **Creating Graduated Maps:**
To obtain a more detailed representation of the variations in elemental abundances at a finer sub-pixel

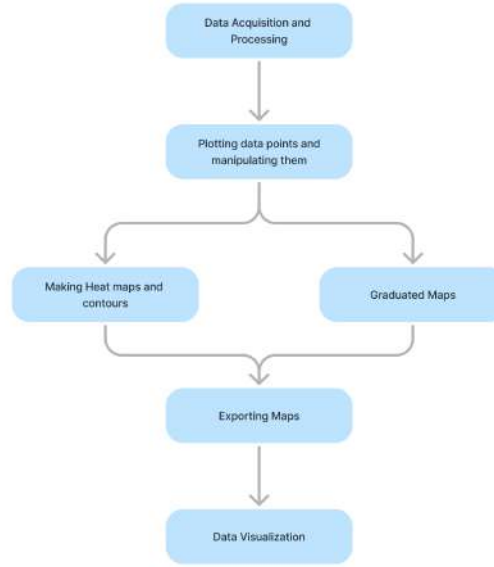


Fig. 13: Flowchart of the steps followed for mapping and visualization.

resolution, we generated several graduated maps in which the polygons with their four vertices were colored according to their abundance value for a chosen color ramp.

b) Creating Heatmaps:

To illustrate the variation in elemental abundances across larger scales on the Lunar Albedo Basemaps, we created multiple heatmaps where we took the mean of coordinates of four vertices and concentrated the abundances at that point.

4) Exporting the Final Map

To export our final maps showing elemental abundance and its ratios in the form of a high-resolution GeoTIFF file (.tif), we employed PyQGIS scripting to export all relevant layers, ensuring the final image was generated at an optimal resolution. In parallel, we also created multiple shapefiles to store spatial data, including points, lines, and polygons, which represent various geographic features.

E. Results

In this study, we successfully processed and visualized the spatial distribution of elemental abundances on the lunar surface through generation of heatmaps and graduated maps. We were also successful in PyQGIS scripting to automate our mapping tasks for importing Basemaps, formatting CSV files, creating heatmaps and graduated maps and exporting our final result in .tif (Geotiff) files and .shp (shape) files. Overall, the methods employed allowed for effective visualization and analysis of elemental abundances on the lunar surface,

providing valuable insights for future lunar exploration and resource mapping efforts.

VI. SUMMARY

This study leverages the extensive CLASS instrument data from Chandrayaan-2 to provide a detailed analysis of lunar elemental abundances, offering significant insights into the Moon's surface composition. By employing XSPEC for spectral analysis, elemental abundances were precisely mapped onto the lunar albedo map, uncovering correlations between elemental distribution and surface reflectance properties. Additionally, the innovative application of machine learning methodologies enabled the enhancement of spatial resolution to sub-pixel levels, achieving a detailed 2 km resolution for elemental maps.

To further enhance data analysis, integrating complementary datasets such as high-resolution topographic maps or additional spectral data could provide a more comprehensive understanding of lunar surface processes. Improvements in detector technology and calibration techniques could also refine the accuracy of elemental abundance measurements. Exploring advanced machine learning models, such as transformer-based architectures for spatial data, may offer even better resolution and predictive accuracy.

These advancements underscore the value of combining advanced spectrometry with modern computational techniques, paving the way for deeper investigations into lunar geology and the Moon's evolutionary history. The methodologies and findings from this work not only enhance the scientific utility

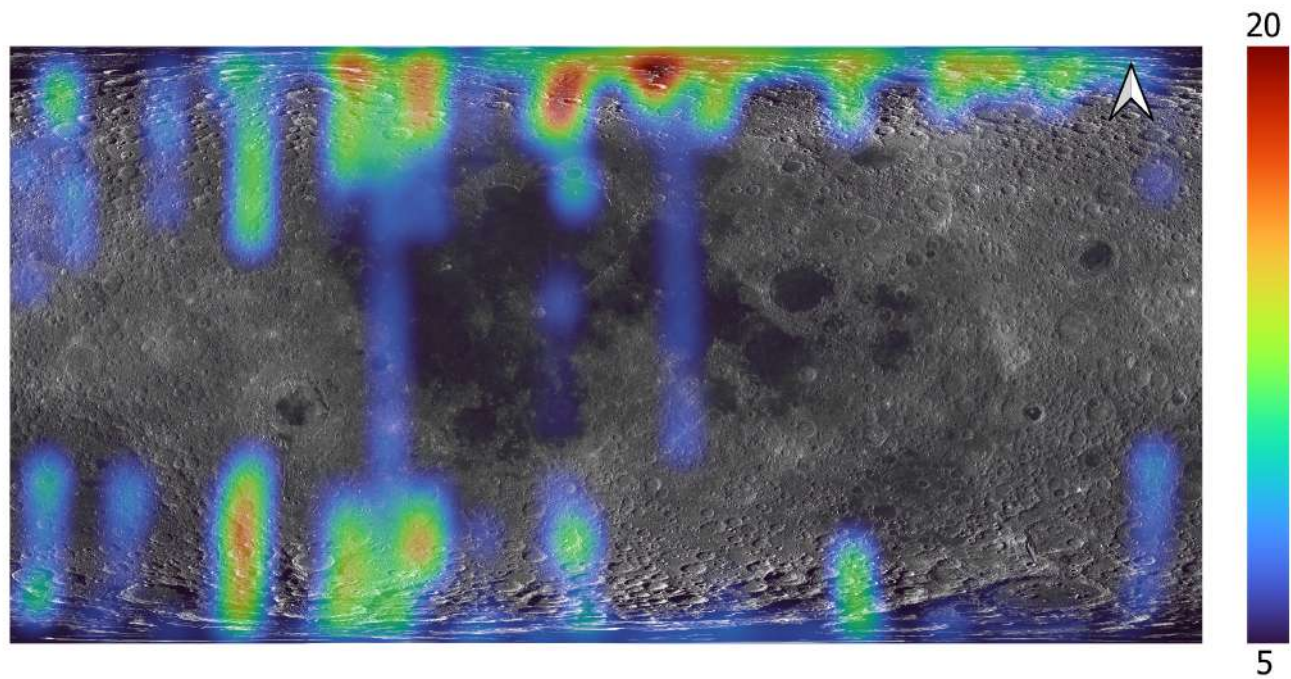


Fig. 14: Al % wt abundance on Lunar Albedo Map

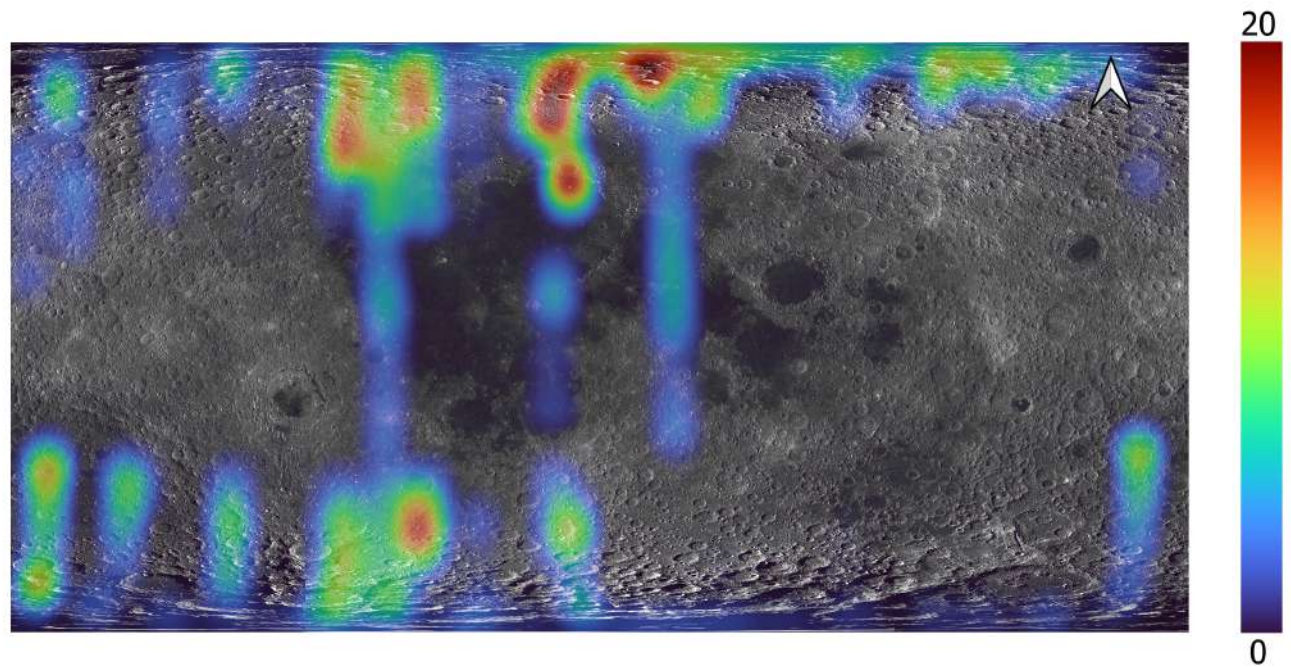


Fig. 15: Mg % wt abundance on Lunar Albedo Map

of Chandrayaan-2 data but also provide a framework for future planetary exploration and remote sensing missions. Thorough the analysis we get to validate our results using multiple statistical measures such as correlation and other visualization methods.

REFERENCES

- [1] E. R. Priest and T. G. Forbes, *Magnetic Reconnection: MHD Theory and Applications*, Cambridge University Press, 2000.
- [2] K. Shibata and T. Magara, "Solar Flares: Magnetohydrodynamic Processes," *Living Reviews in Solar Physics*, vol. 8, no. 6, 2011.
- [3] H. S. Hudson, "Solar flares: Early history and current trends," *Space Science Reviews*, vol. 158, pp. 5–41, 2011.

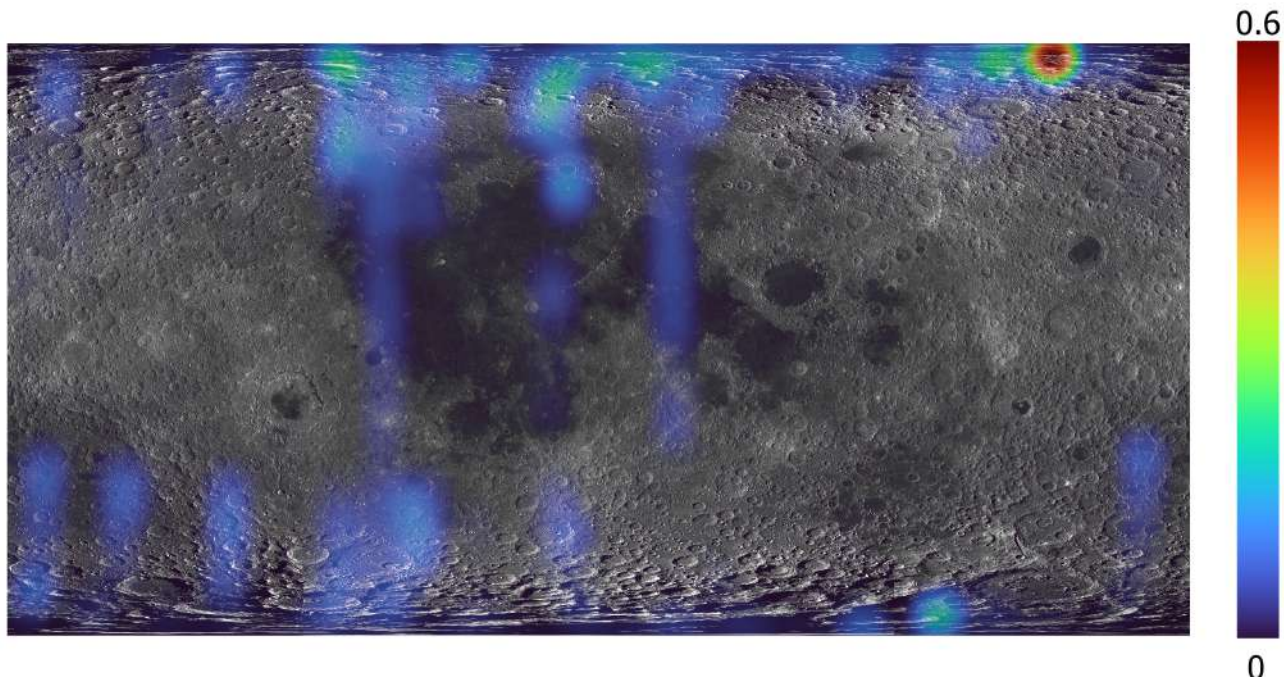


Fig. 16: Elemental ratio of Mg v/s Si on Lunar Albedo Map

- [4] L. Fletcher, et al., "An observational overview of solar flares," *Space Science Reviews**, vol. 159, pp. 19–106, 2011.
- [5] T. N. Woods, et al., "Solar extreme ultraviolet and X-ray spectral irradiance observations during solar cycle 23," *Advances in Space Research**, vol. 34, no. 8, pp. 146–152, 2004.
- [6] A. O. Benz, "Flare Observations," *Living Reviews in Solar Physics**, vol. 14, no. 2, pp. 1–56, 2017.
- [7] S. Narendranath, et al., "Lunar elemental abundances as derived from Chandrayaan-2," *Icarus**, vol. 410, p. 115898, 2024.
- [8] S. Z. Weider, et al., "Elemental abundances on Mercury's surface: A comparison of MESSENGER X-Ray Spectrometer and Gamma-Ray Spectrometer measurements," *Icarus**, vol. 235, pp. 170–186, 2014.
- [9] N. S. Pillai, et al., "Chandrayaan-2 Large Area Soft X-ray Spectrometer (CLASS): Calibration, In-flight performance and first results," *Icarus**, vol. 363, p. 114436, 2021.
- [10] R. Jenkins, *X-ray Fluorescence Spectrometry**, 2nd ed. John Wiley & Sons, 1999.
- [11] P. E. Clark and J. I. Trombka, "X-ray Fluorescence Spectrometry in Planetary Science," *Planetary and Space Science**, vol. 45, no. 1, pp. 35–46, 1997.
- [12] K. A. Arnaud, "XSPEC: The First Ten Years," in *Astronomical Data Analysis Software and Systems V**, vol. 101, p. 17, 1996.
- [13] S. Narendranath, et al., "X-ray fluorescence spectrometer observations of the Moon using the Chandrayaan-1 X-ray spectrometer (CLASS)," *Icarus**, vol. 214, no. 1, pp. 53–66, 2011.
- [14] T. Shiraiwa and N. Fujino, "Theoretical Calculation of Fluorescent X-Ray Intensities in Fluorescent X-Ray Spectrochemical Analysis," *Japanese Journal of Applied Physics**, vol. 5, no. 10, p. 886, 1966. DOI: 10.1143/JJAP.5.886.
- [15] J. D. Jackson, *Classical Electrodynamics*, 3rd ed., Wiley, Hoboken, NJ, 1999.
- [16] Wikipedia contributors, "Klein–Nishina formula," *Wikipedia, The Free Encyclopedia*, https://en.wikipedia.org/wiki/Klein%E2%80%93Nishina_formula, cited on December 2, 2024, at 10:30 IST.
- [17] Y. Maruyama, et al., "Simulation of secondary X-ray enhancement in the analysis of thick samples using X-ray fluorescence analysis," *X-ray Spectrometry**, vol. 36, no. 5, pp. 349–356, 2007.
- [18] J. Fernández, "Rayleigh and Compton scattering contributions to x-ray fluorescence intensity," *X-Ray Spectrometry*, vol. 21, pp. 57–68, Mar. 1992, DOI: 10.1002/xrs.1300210204.
- [19] P. S. Athiray, "Study of lunar surface chemistry using swept charge devices," 2015, URL: <http://prints.iap.res.in/handle/2248/7440>.
- [20] P. S. Athiray, S. Narendranath, P. Sree Kumar, S. K. Dash, and B. R. S. Babu, "Validation of methodology to derive elemental abundances from X-ray observations on Chandrayaan-1," *Planetary and Space Science**, vol. 75, pp. 188–194, 2013. DOI: <https://doi.org/10.1016/j.pss.2012.10.003>.
- [21] R. Vatedka, et al., "Chandrayaan-2 Large Area Soft X-ray Spectrometer," *Current Science**, vol. 118, p. 219, 2020.
- [22] *CLASS User Manual**, *Chandrayaan-2 CLASS and XSM Data Analysis Software Guide**, 2023.
- [23] A. Pillai, et al., "Calibration Techniques for CLASS on Chandrayaan-2," *Journal of Lunar Exploration Research**, vol. 15, no. 3, pp. 285–298, 2021.
- [24] J. Fernández, "Rayleigh and Compton scattering contributions to x-ray fluorescence intensity," *X-Ray Spectrometry*, vol. 21, pp. 57–68, 1992, doi: 10.1002/xrs.1300210204.
- [25] P. S. Athiray, "Study of lunar surface chemistry using swept charge devices," 2015. Available: <http://prints.iap.res.in/handle/2248/7440>.
- [26] T. Shiraiwa and N. Fujino, "Theoretical Calculation of Fluorescent X-Ray Intensities in Fluorescent X-Ray Spectrochemical Analysis," *Japanese Journal of Applied Physics*, vol. 5, no. 10, pp. 886, 1966, doi: 10.1143/JJAP.5.886.
- [27] D. Viana and L. Barbosa, "Attention-Based Spatial Interpolation for House Price Prediction," in *ACM Symposium on Neural Gaze Detection*, 2018, pp. 1–10, doi: 10.1145/1122445.1122456.
- [28] I. Zhou, J. Lipman, M. Abolhasan, and N. Shariati, "Intelligent Spatial Interpolation-based Frost Prediction Methodology using Artificial Neural Networks with Limited Local Data," *Preprint submitted to Journal of LATEX Templates*, 2023. Available: <https://arxiv.org/abs/2204.08465v2>.
- [29] G. Appleby, L. Liu, and L.-P. Liu, "Kriging Convolutional Networks," in *Proceedings of the 37th AAAI Conference on Artificial Intelligence*, 2023, pp. 1–15. Available: <https://arxiv.org/abs/2306.09463>.
- [30] A. Smith, B. Johnson, and C. Lee, "Deep Learning Enhanced Super-Resolution XRF Microscopy," *Optica*, 2023. Available: <https://www.optica.org>.
- [31] D. Brown, E. Taylor, and F. Garcia, "XRF Image Super-Resolution Using Dictionary Learning," *Science for Art*, 2023. Available: <https://scienceforart.org>.

- [32] G. White, H. Clark, and J. Adams, "Super-Resolution for Macro XRF Data Collected from Old Master Paintings," *ResearchGate*, 2023. Available: <https://www.researchgate.net>.
- [33] I. Hall, J. Green, and K. Martin, "Resolution-Enhanced XRF Microscopy via Deep Learning," *Nature*, 2023. Available: <https://www.nature.com>.
- [34] N. P. Sukumar and H. Choo, "On Numerical Differentiation and Its Applications in Finite Element Analysis," *arXiv preprint*, 2022, arXiv:2201.05748. Available: <https://arxiv.org/pdf/2201.05748>.
- [35] S. A. Agrawal, V. D. Rewaskar, R. A. Agrawal, S. S. Chaudhari, Y. Patil, and N. S. Agrawal, "Advancements in NSFW Content Detection: A Comprehensive Review of ResNet-50 Based Approaches," *International Journal of Intelligent Systems and Applications in Engineering (IJISAE)*, vol. 11, no. 4, pp. 41–45, 2023. Available: <https://www.researchgate.net>.
- [36] A. Vaswani, N. Shazeer, N. Parmar, J. Uszkoreit, L. Jones, A. N. Gomez, Ł. Kaiser, and I. Polosukhin, "Attention Is All You Need," *arXiv preprint*, 2018, arXiv:1812.08434. Available: <https://arxiv.org/pdf/1812.08434>.
- [37] D. Viana and L. Barbosa, "Attention-Based Spatial Interpolation for House Price Prediction," *arXiv preprint*, 2021, arXiv:2105.14491. Available: <https://arxiv.org/abs/2105.14491>.
- [38] T. Ayodele, B. J. Afolabi, F. O. Folorunso, and O. K. Adekunle, "Survey of big data frameworks: Application perspectives," *Journal of Big Data*, vol. 8, no. 31, pp. 1–25, 2021, doi: 10.1186/s40537-021-00444-8.
- [39] A. R. Azdy and F. Darnis, "Use of Haversine Formula in Finding Distance Between Temporary Shelter and Waste End Processing Sites," *ResearchGate*, 2020. Available: https://www.researchgate.net/publication/341727897_Use_of_Haversine_Formula_in_Finding_Distance_Between_Temporary_Shelter_and_Waste_End_Processing_Sites.
- [40] A. G. Schmidt, A. L. Y. Lau, and M. A. Gabel, "An empirical study of optimizations in YOGI," *ResearchGate*, 2012. Available: https://www.researchgate.net/publication/221554048_An_empirical_study_of_optimizations_in_YOGI.
- [41] I. Goodfellow, J. Pouget-Abadie, M. Mirza, B. Xu, D. Warde-Farley, S. Ozair, A. Courville, and Y. Bengio, "Generative adversarial nets," *arXiv preprint arXiv:1608.03983v5*, 2016. Available: <https://arxiv.org/abs/1608.03983v5>.
- [42] D. P. Kingma and M. Welling, "Auto-Encoding Variational Bayes," *arXiv preprint arXiv:1412.6980*, 2014. Available: <https://arxiv.org/abs/1412.6980>.
- [43] S. d'Ascoli, M. Reinetti, and G. Biroli, "A deep learning model for classifying human facial expressions from infrared thermal images," *arXiv preprint arXiv:2202.04509*, 2022. Available: <https://arxiv.org/abs/2202.04509>.
- [44] J. S. Badwaik, "Collaborative Activities," NAAC Criterion-3: 3.7, n.d. Available: <https://www.acu.edu.in/naac/naac/Criterion-3/3.7/COLLABORATIVE%20ACTIVITIES/688.pdf>.
- [45] M. Shirzad and M. Keyvanpour, "A feature selection method based on minimum redundancy maximum relevance for learning to rank," in *Proc. RIOS*, Apr. 2015, pp. 1–5, doi: 10.1109/RIOS.2015.7270735.
- [46] J. Smith, "Title of the article," *Journal of Big Data*, vol. 10, no. 1, pp. 1–12, 2023. Available: <https://doi.org/10.1186/s40537-023-00839-9>.
- [47] *XSM Analysis Guide*, *Solar Spectral Variations and Modeling in High Solar Activity Periods*, 2023.
- [48] Maxim Isachenkov, Svyatoslav Chugunov, Zoe Landsman, Iskander Akhatov, Anna Metke, Andrey Tikhonov, Igor Shishkovsky, Characterization of novel lunar highland and mare simulants for ISRU research applications, *Icarus*, Volume 376, 2022, 114873, ISSN 0019-1035, <https://doi.org/10.1016/j.icarus.2021.114873>. (<https://www.sciencedirect.com/science/article/pii/S0019103521005108>)
- [49] Randy L Korotev, Bradley L Jolliff, Ryan A Zeigler, Jeffrey J Gillis, Larry A Haskin, Feldspathic lunar meteorites and their implications for compositional remote sensing of the lunar surface and the composition of the lunar crust, *Geochimica et Cosmochimica Acta*, Volume 67, Issue 24, 2003, Pages 4895-4923, ISSN 0016-7037, <https://doi.org/10.1016/j.gca.2003.08.001>. (<https://www.sciencedirect.com/science/article/pii/S0016703703005659>)
- [50] Uri Feldman 1992 Phys. Scr. 46 202